The Astrophysical Journal, 978:39 (20pp), 2025 January 01 https://doi.org/10.3847/1538-4357/ad9820

Stellar Metallicities from DECam *u*-band Photometry: A Study of Milky Way Ultra-faint Dwarf Galaxies

Yue Pan[1,2], Anirudh Chiti[1,3], Alex Drlica-Wagner[1,3,4], Alexander P. Ji[1,3], Ting S. Li[5,6], Guilherme Limberg[1,3,7], Douglas L. Tucker[4], and Sahar Allam[4]
[1] Department of Astronomy & Astrophysics, University of Chicago, 5640 S Ellis Avenue, Chicago, IL 60637, USA
[2] Department of Astrophysical Sciences, Princeton University, Princeton, NJ 08544, USA
[3] Kavli Institute for Cosmological Physics, University of Chicago, Chicago, IL 60637, USA
[4] Fermi National Accelerator Laboratory, P.O. Box 500, Batavia, IL 60510, USA
[5] David A. Dunlap Department of Astronomy & Astrophysics, University of Toronto, 50 St. George Street, Toronto, ON, M5S3H4, Canada
[6] Dunlap Institute for Astronomy & Astrophysics, University of Toronto, 50 St George Street, Toronto, ON M5S 3H4, Canada
[7] Universidade de São Paulo, IAG, Departamento de Astronomia, SP 05508-090, São Paulo, Brazil
Received 2024 April 11; revised 2024 November 19; accepted 2024 November 20; published 2024 December 26

Abstract

We conducted an in-depth analysis of candidate member stars located in the peripheries of three ultra-faint dwarf (UFD) galaxy satellites of the Milky Way (MW): Boötes I (Boo1), Boötes II (Boo2), and Segue I (Seg1). Studying these peripheral stars has previously been difficult due to contamination from the MW foreground. We used *u*-band photometry from the Dark Energy Camera (DECam) to derive metallicities to efficiently select UFD candidate member stars. This approach was validated on Boo1, where we identified both previously known and new candidate member stars beyond five half-light radii. We then applied a similar procedure to Boo2 and Seg1. Our findings hinted at evidence for tidal features in Boo1 and Seg1, with Boo1 having an elongation consistent with its proper motion and Seg1 showing some distant candidate stars, a few of which are along its elongation and proper motion. We find two Boo2 stars at large distances consistent with being candidate member stars. Using a foreground contamination rate derived from the Besançon Galaxy model, we ascribed purity estimates to each candidate member star. We recommend further spectroscopic studies on the newly identified high-purity members. Our technique offers promise for future endeavors to detect candidate member stars at large radii in other systems, leveraging metallicity-sensitive filters with the Legacy Survey of Space and Time and the new, narrowband Ca HK filter on DECam.

Unified Astronomy Thesaurus concepts: Dwarf galaxies (416); Stellar populations (1622); Galaxy evolution (594)

Materials only available in the online version of record: machine-readable tables

1. Introduction

Over the last two decades, large digital sky surveys such as the Sloan Digital Sky Survey (SDSS), the Dark Energy Survey (DES), and PanSTARRS have allowed astronomers to identify many more low surface brightness stellar systems surrounding the Milky Way (MW; e.g., J. D. Simon 2019). Among these faint stellar systems, ultra-faint dwarf galaxies (UFDs), which were first detected in SDSS data two decades ago (B. Willman et al. 2005a, 2005b), have generated particular interest due to their extremely faint luminosities ($L < 10^5 L_\odot$), chemically primitive compositions ([Fe/H] $\lesssim -2.0$), large dark-matter contents ($\gtrsim 100 M_\odot/L_\odot$; J. D. Simon & M. Geha 2007), and old ages (~13 Gyr; e.g., T. M. Brown et al. 2014; J. D. Simon 2019).

As per the hierarchical structure formation theory of galaxies, smaller galaxies are formed before larger ones (S. D. M. White & C. S. Frenk 1991; S. Cole et al. 2000). Therefore, UFDs are presumably the building blocks of more massive galaxies and particularly interesting probes of the early chemical evolution of the Universe since they are thought to have undergone only a few cycles of chemical enrichment (A. Frebel et al. 2014). The number and distribution of UFDs can constrain dark-matter models (e.g., S. Y. Kim et al. 2018; E. O. Nadler et al. 2021; S. Mau et al. 2022). Moreover, the resolved kinematics of their member stars link to a number of questions related to dark matter and can be used to put constraints on the dark-matter annihilation cross sections and the dark-matter distribution on small scales (F. Calore et al. 2018; H. Abdallah et al. 2020; K. Malhan et al. 2022).

More than 50 UFDs have been discovered around the MW. While their relative proximity (<200 kpc) makes them suitable for in-depth investigations, it is still extremely hard to study their resolved stellar populations due to their faint nature. Traditionally, member stars of MW UFDs are identified by low- and medium-resolution spectroscopy, through the clustered radial velocities and low metallicities of UFD members. Subsequently, one can derive the dynamical mass from the velocity dispersion of member stars (M. G. Walker et al. 2009; J. Wolf et al. 2010) and use the estimated mass-to-light ratio to distinguish UFDs from globular clusters (GCs; B. Willman & J. Strader 2012). One can also distinguish UFDs from GCs through metallicity measurements since UFDs show significant metallicity spreads (e.g., A. Frebel et al. 2014), whereas GCs generally show minimal spreads ($\lesssim$0.05 dex; e.g., E. Carretta et al. 2009).

However, spectroscopy of UFDs is primarily devoted to their central regions ($\lesssim$2 half-light radii), since member stars in the outskirts are sparsely distributed (R. R. Muñoz et al. 2018) and dominated by MW foreground stars. Simulations suggest that UFDs are formed within extended dark-matter halos and may

Table 1
Observations of Boo1, Boo2, and Seg1

Name	R.A. (h:m:s)	Decl. (d:m:s)	UT Observation Dates	Instrument	Filter	Seeing	Exposure Time (s)
Boo1	14:00:06.0	+14:30:00	2021 Mar 12	DECam	u	1.″0	20 × 300 s
Boo2	13:58:00.0	+12:51:00	2021 Jun 10	DECam	u	1.″0	20 × 300 s
Seg1	10:07:04.0	+16:04:55	2021 Jun 10	DECam	u	1.″0	20 × 300 s

be shaped by early galaxy mergers and supernova feedback (A. Deason et al. 2014; F. Munshi et al. 2019; C. Wheeler et al. 2019). Signatures of these effects would primarily reside in the outer regions of UFDs. Thus, a more efficient method to identify member stars in the outer regions of dwarf galaxies is needed to understand early dwarf galaxy evolution and probe the nature of their small-scale dark-matter halos.

The efficiency of spectroscopy can be improved by using photometry to determine metallicities and identify candidate member stars. In the 1980s, a narrowband filter on the Curtis Schmidt telescope at Cerro Tololo Inter-American Observatory (CTIO), targeting the H and K lines of Ca II, was employed to identify metal-poor stars (e.g., T. C. Beers et al. 1985). Additionally, early research by B. J. Anthony-Twarog et al. (1991) demonstrated the effectiveness of photometry in detecting metal-poor stars. More recently, A. B. Pace & T. S. Li (2019) showed that metallicity-sensitive broadband colors from DES can enhance the efficiency of identifying member stars in UFD galaxies. Recent studies have further generalized this approach using intermediate and narrowband filters to identify UFD stars (A. Chiti et al. 2020, 2021; N. Longeard et al. 2021, 2022, 2023; S. W. Fu et al. 2023). Current iterations of photometric metallicity work typically determine the metallicity by establishing a relation between a star's metallicity and its brightness in a narrowband imaging filter that encompasses a prominent metal absorption feature (e.g., Ca II K line; S. C. Keller et al. 2007; E. Starkenburg et al. 2017). This technique offers the advantage of determining metallicities for all stars within the camera's field of view (FOV), unlike spectroscopy, which has to be more targeted and is constrained by factors like slit arrangements and the number of fibers.

In this paper, we combine targeted u-band observations from the Dark Energy Camera (DECam) with additional broadband photometry from DECam Local Volume Exploration Survey (DELVE) Data Release 2 (DR2; A. Drlica-Wagner et al. 2022) and astrometry from the Gaia DR3 catalog (Gaia Collaboration et al. 2016, 2023) to identify candidate member stars of three MW UFDs: Boötes I (Boo1), Boötes II (Boo2), and Segue I (Seg1). The DECam u band covers the prominent Ca II K metal absorption line and thus can be used to derive photometric metallicities. Since Boo1 is the most widely studied MW UFD in our sample, we start by identifying candidate member stars of Boo1 and comparing our photometric catalog to existing spectroscopic catalogs. We then statistically evaluate the purity (i.e., cleanness from nonmember stars) and completeness of our sample and generalize our method to the other two systems to identify new candidate member stars out to large radii. We demonstrate the power of DECam u-band photometry to identify low-metallicity stars, we identify low-metallicity stars in the outskirts of each UFD, and we publicly release our selected low-metallicity UFD candidate member stars to facilitate spectroscopic follow-up work.

This paper is organized as follows. Section 2 outlines our DECam u-band observations, data reduction, and zero-point calibration. Section 3 presents our candidate member star selection process, which combines an isochrone selection, a proper-motion selection, and a photometric metallicity selection. Section 4 presents our investigation of stars in the outskirts of Boo1, Boo2, and Seg1, along with a discussion of the completeness and purity of the sample. Finally, Section 5 discusses the relation of the candidate member star spatial distribution to the evolution nature of UFDs, and Section 6 summarizes our main findings.

2. Observations and Data Reduction

In this section, we discuss our observations and the process of producing source catalogs used in our subsequent analysis. We present the DECam u-band observations in Section 2.1, the data reduction and generation of source catalogs from individual u-band exposures in Section 2.2, and the procedure for calibrating u-band zero-points and generating a combined source catalog in Section 2.3. Our final, combined u-band catalog is then cross-matched with DELVE DR2 (A. Drlica-Wagner et al. 2022) for broadband g, i photometry that is used in subsequent analyses.

2.1. Observations

We obtained u-band photometry of Boo1, Boo2, and Seg1 using DECam (B. Flaugher et al. 2015) on the 4 m Blanco Telescope located at CTIO in Chile (PI: Ji, PropID: 2021A-0272). The DECam hosts 62 2048 × 4096 pixel science CCDs that have a pixel scale of ~0.″26 pixel^{-1}. This grants DECam a large FOV (~3 deg^2, ~2.°2 across), making it ideally suited for wide-field photometric studies. We observed each of the aforementioned dwarf galaxies using sequences of 300 s exposures dithered by 30.″0 to cover chip gaps. Total exposure times were calculated to target 0.03 mag precision at $u = 23$. Conditions were clear and the seeing was stable at ~1.″0 throughout observations. Table 1 displays the full details of our observations.

2.2. DECam u-band Data Reduction and Photometry

The DECam data were processed with the DES Data Management Final Cut pipeline (E. Morganson et al. 2018). This pipeline includes includes bias subtraction, nonlinearity corrections, bad pixel masking, gain correction, brighter-fatter correction, and flat-fielding. Bias corrections and flat-fielding made use of "super-cal" assembled by combining flats and biases taken over several nights developed for u-band data processing for the DES Deep Fields (W. G. Hartley et al. 2022). In addition, the DES Final Cut pipeline includes identification and masking of cosmic rays, bleed trails from saturated stars, and trails from artificial satellites. Sky background estimation was performed through principal component analysis decomposition over the entire focal plane following

G. M. Bernstein et al. (2017), and then adjusted CCD by CCD during source extraction and measurement.

Astronomical source detection and measurement were performed on a per CCD basis using the PSFEx and SourceExtractor routines (E. Bertin & S. Arnouts 1996; E. Bertin 2011). As part of this step, astrometric calibration was performed with SCAMP (E. Bertin 2006) by matching objects to the Gaia DR2 catalog (Gaia Collaboration et al. 2018). The SourceExtractor source detection threshold was set to detect sources with signal-to-noise ratio S/N > 5. Photometric fluxes and magnitudes refer to the SourceExtractor point-spread function (PSF) model fit.

2.3. DECam u-band Zero-point Calibration

We calibrate the photometric zero-points for the DECam u-band source catalogs generated in Section 2.2 by comparing instrumental DECam u-band magnitudes with predicted DECam u-band magnitudes derived from u-, g-, and r-band photometry from the SDSS DR16 catalog (R. Ahumada et al. 2020). Specifically, DECam u-band magnitudes can be related to SDSS u-, g-, and r-band magnitudes using the following equation (A. Tucker et al. 2024, in preparation):

$$u_{\rm DECam} = u_{\rm SDSS} - 0.479 + 0.466 \cdot (g-r)_{\rm SDSS} - 0.35 \cdot (g-r)^2_{\rm SDSS} \quad (1)$$

for objects with $0.2 \leqslant (g-r)_{\rm SDSS} \leqslant 1.2$. This process is similar to the SDSS g-, r-, i-, and z-band magnitude conversion to DES magnitudes in Appendix B.1 of T. M. C. Abbott et al. (2021), but with a second-order term. The zero-point can then be estimated to be the median difference between the DECam u-band magnitudes in our catalogs and the DECam u-band predicted from SDSS photometry.

To obtain the SDSS u-, g-, and r-band magnitudes for sources in our catalogs, we cross-match our catalogs from Section 2.2 with the SDSS DR16 catalog (R. Ahumada et al. 2020) using R.A. and decl. with a radius of 1.″0. To ensure a clean estimate of the zero-point, we: (1) retain objects that have a u-band magnitude error of less than 0.1 mag in both our catalog and the SDSS DR16 catalog; (2) retain objects with no photometric flags in either catalog (FLAGS = 0, FLAGS_WEIGHT = 0, and IMAFLAGS_ISO = 0; these flags mean that there are no known photometric and weighting issues, and the quality of the isophotal analysis used to measure the brightness profile is good); and (3) exclude galaxies with |SPREAD_MODEL| < 0.003 + SPREADERR_MODEL (this flag is commonly used to distinguish between stars and galaxies based on the shape of their light profiles; S. E. Koposov et al. 2015; C. T. Slater et al. 2020). After this selection, we calculate a first-pass u-band zero-point offset for each individual chip in each exposure by taking the median offset between the u-band magnitudes in Section 2.2 and those predicted by SDSS photometry. We then clip all sources that are $>3\sigma$ outliers relative to this zero-point and recalculate as before to obtain zero-points for each chip and exposure. The median ($\rm ZP_i$) and standard deviation ($\rm ZP_{err,i}$) of zero-points after sigma clipping are the zero-point value and error for each exposure. The typical number of stars on each chip used for the zero-point estimate is ~30–40. The left panel of Figure 1 shows the distribution of inferred zero-points from individual stars for all 60 chips for 20 300 s exposures. Each curve is the median value of zero-points for all 60 chips at a single exposure. The shift of these distributions indicate atmospheric variations during different exposure times. The right panel shows the median zero-point values for all 60 chips at one single exposure. The variations here indicate the different quantum efficiencies of different detectors.

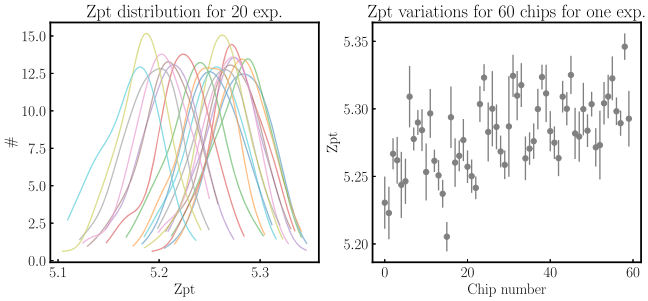

Figure 1. Left: smoothed zero-point distribution for all 60 chips across all 20 exposures. The zero-point is defined as the theoretical DECam u-band magnitude from the SDSS DR16 catalog minus the observed DECam u-band magnitude. Each curve represents the distribution of median zero-point values for all stars across the 60 chips in a single exposure, illustrating atmospheric variations across the 20 exposures. Right: median zero-point values with error bars across all 60 chips for a single exposure, highlighting the differences in quantum efficiencies among detectors.

For each source in our catalog, we take the weighted average of its zero-point-corrected magnitude across 20 exposures to obtain a final u-band magnitude. Note that this is just a weighted average of the measured magnitudes for each star instead of doing photometry on a coadded image. To start with, for each exposure, we concatenate the catalog of all sources in each chip. We then cross-match between the 20 exposures to generate a final catalog. We note that not every star may be detected in each exposure, due to varying weather conditions at the time of each exposure, pixel artifacts, or statistical fluctuations for sources near the detection threshold.

We calculate the calibrated DECam u-band magnitude based on the zero-point correction in each exposure ($MAG\_PSF+\rm ZP_i$) for each selected star in all 20 exposures. Typical values of $\rm ZP_i$ vary between ~5.1 and ~5.3 depending on the weather condition. The random uncertainty associated with this calibrated magnitude is computed as the quadratic sum of the uncertainties from the DECam u-band measurement (MAG_PSF_ERR) and the zero-point calculation ($\rm ZP_{err,i}$) for each exposure. In the bright limit $g < 18.5$, the stars' u-band magnitude error will be dominated by the zero-point calibration precision. We find the standard deviation of u-band magnitudes in this regime to be ~0.035 mag across the 20 exposures. We take this to be our zero-point calibration uncertainty, and we add this value in quadrature to our random u-band magnitude uncertainty to derive a total photometric uncertainty, which will be propagated when computing photometric metallicity uncertainties.

We compute the mean of the calibrated magnitudes for all selected objects across all exposures using the inverse-variance weighting method (T. Strutz 2010):

$$\mu = \frac{\sum_{i=1}^{20} x_i/\sigma_i^2}{\sum_{i=1}^{20} 1/\sigma_i^2} \quad (2)$$

where x_i and σ_i are the calibrated DECam u-band magnitude ($MAG\_PSF+\rm ZP_i$) and the quadratic sum of MAG_PSF_ERR and $\rm ZP_{err,i}$, respectively, for each exposure. The variance

Table 2
Properties of Boo1, Boo2, and Seg1

Name	r_h (′)	$\mu_\alpha \cos\delta$ (mas yr^{-1})	μ_δ (mas yr^{-1})	$(m-M)_o$	θ (deg)	ϵ	References
Boo1	9.97 ± 0.27	−0.39 ± 0.01	−1.06 ± 0.01	19.11	6.0 ± 3.0	0.30 ± 0.03	(a, b, b, c, a, a)
Boo2	3.17 ± 0.42	$-2.33^{+0.09}_{-0.08}$	−0.41 ± 0.06	18.10	−68.0 ± 27.0	0.25 ± 0.11	(a, b, b, d, a, a)
Seg1	3.62 ± 0.42	−2.21 ± 0.06	−3.34 ± 0.05	16.80	77.0 ± 15.0	0.33 ± 0.10	(a, b, b, e, a, a)

References. (a) R.R. Muñoz et al. (2018); (b) A. W. McConnachie & K. A. Venn (2020); (c) M. Dall'Ora et al. (2006); (d) S. M. Walsh et al. (2008); (e) V. Belokurov et al. (2007).

among all weighted averages is then computed as in T. Strutz (2010):

$$\sigma^2(\mu) = \frac{1}{\sum_{i=1}^{20} 1/\sigma_i^2}. \quad (3)$$

3. Selecting Candidate Member Stars Using Photometric Metallicity

After obtaining the calibrated DECam *u*-band magnitudes for all objects in our catalog, we apply several selection criteria to identify a reasonably pure sample of potential UFD member stars. First, we apply `parallax_over_error` < 3 to weed out sources with resolved parallax values (i.e., nearby foreground stars). Second, we perform an isochrone cut along the color–magnitude diagram (CMD) of each UFD using DELVE DR2 photometry (A. Drlica-Wagner et al. 2022; Section 3.1). Third, we apply a proper-motion cut using the Gaia DR3 catalog (Gaia Collaboration et al. 2023) to identify stars with kinematics similar to each UFD (Section 3.2). Finally, we identify low-metallicity stars using the DECam *u*-band magnitude and corresponding *g*, *i* magnitudes since UFD stars are more metal-poor compared to MW foreground stars (Section 3.3).

3.1. Isochrone Cut

We begin by applying an isochrone cut to select stars that exhibit a consistent CMD with that of an old, metal-poor population at the distance of Boo1 (see Table 2). We first use `STILTS` to cross-match the final catalog obtained in Section 2.3 with the DELVE DR2 catalog (A. Drlica-Wagner et al. 2022) to obtain precise DECam *g*- and *i*-band magnitudes (*MAG_PSF_g*, *MAG_PSF_i*). To determine the reddening correction for each star, we use dust maps from D. J. Schlegel et al. (1998) to obtain $E(B-V)$ values. The reddening coefficients for *u*, *g*, and *i* bands are taken as $R_u = 3.995$,[8] $R_g = 3.186$, and $R_i = 1.569$, respectively, following T. M. C. Abbott et al. (2018) to convert $E(B-V)$ to the reddening corrections A_g and A_i. We apply this correction to the DELVE magnitudes to obtain the dereddened *g*-, *i*-, and *u*-band magnitudes.

After obtaining dereddened *g*- and *i*-band magnitudes for all selected stars, we fit the *g*, $g-i$ CMD with an isochrone of [Fe/H] = −2.49 and age = 13 Gyr from the Dartmouth Stellar Evolution Database (A. Dotter et al. 2008) at a distance modulus of $m-M = 19.1$ (A. W. McConnachie 2012), which has been shown to represent the stellar population of Boo1 well. We then select stars that have a $g-i$ color within 0.2 mag of this isochrone. The left panel of Figure 2 illustrates the selection procedure based on the isochrone.

[8] Taken from https://www.legacysurvey.org/dr8/catalogs/.

3.2. Proper-motion Cut

The proper-motion cut is carried out by selecting stars that have proper motions consistent with the systemic proper motion of Boo1. We cross-match the catalog of stars that passed our isochrone cut in Section 3.1 with the Gaia DR3 catalog (Gaia Collaboration et al. 2023) to obtain proper-motion data and corresponding uncertainties for our selected stars. We apply a reflex correction on both the proper motions of stars and the systemic proper motion of the UFD from A. W. McConnachie & K. A. Venn (2020). The systemic proper motion after our reflex correction is visually consistent with that in Figure 16 of A. B. Pace et al. (2022) for Boo1. We then evaluate the consistency of these proper motions with the proper motion of Boo1 obtained from A. W. McConnachie & K. A. Venn (2020) using the Mahalanobis distance (F. Feroz et al. 2009)

$$d_{\rm Mahalanobis} = \sqrt{(\boldsymbol{x}-\boldsymbol{y})^T \cdot \Sigma^{-1} \cdot (\boldsymbol{x}+\boldsymbol{y})} \quad (4)$$

where Σ is the covariance matrix between pmRA and pmDEC obtained from the correlation matrix and the proper-motion errors in Gaia, and $\boldsymbol{x} = (\mathrm{pm}_{\mathrm{R.A.,Boo1}}, \mathrm{pm}_{\mathrm{decl.,Boo1}})$, $\boldsymbol{y} = (\mathrm{pm}_{\mathrm{R.A.}}, \mathrm{pm}_{\mathrm{decl.}})$ for each source. We select stars that have $d_{\rm Mahalanobis} < 3$. The right two panels of Figure 2 illustrate this selection procedure.

3.3. Photometric Metallicities

We outline a photometric method to obtain a star's metallicity based on its DECam *u*-band magnitude and $g-i$ color, which is an efficient way to estimate metallicities for spatially complete samples of stars without requiring traditional spectroscopy. Such a method has been used in studies of dwarf galaxies in the past with, e.g., the SkyMapper *v* filter (A. Chiti et al. 2020, 2021) and the Pristine Ca HK filter (N. Longeard et al. 2021, 2022, 2023). Here, we demonstrate that a similar analysis can be performed with DECam *u*-band photometry due to the Ca II K absorption feature encompassing a fraction of the bandpass of the filter. Figure 3 illustrates a synthetic spectrum overlaid with the DECam *u* band, showing that the DECam *u*-band total throughput covers the prominent Ca II K absorption feature at 3933 Å. Therefore, the higher a star's metallicity, the fainter it will appear in the DECam *u* band at a given effective temperature and surface gravity. Consequently, the strength of the feature (as a function of the metallicity of the star, among other stellar parameters) affects the brightness of the star in the DECam *u* band. We describe our analysis with Boo1 here since it is the most extensively studied system regarding stellar metallicities among the three UFDs we focused on in this study and has evidence of extratidal features (V. Belokurov et al. 2006a; N. F. Martin et al. 2007; J. E. Norris et al. 2008; T. A. Roderick et al. 2016; C. Filion & R. F. G. Wyse 2021; S. A. Jenkins et al. 2021; N. Longeard et al. 2022).

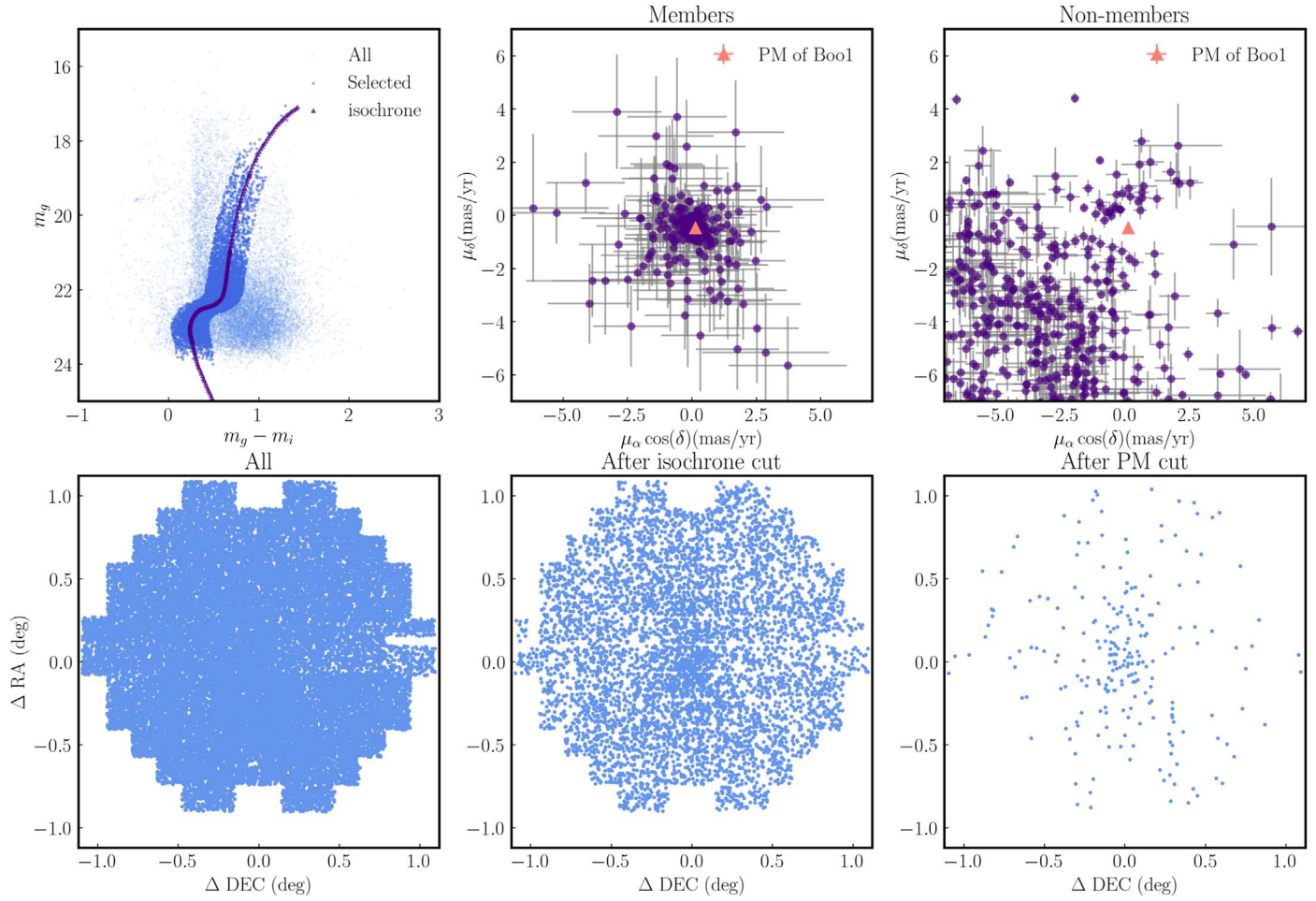

Figure 2. Top: isochrone and proper-motion selection of candidate member stars for Boo1. Top left: the CMD of all stars in our catalog for Boo1 (light blue) and selected stars (dark blue) using the isochrone cuts illustrated in Section 3. The isochrone of metallicity [Fe/H] = −2.49, age = 13 Gyr, and distance modulus of 19.1 is shown as purple. We select stars that have a $g - i$ color within 0.2 mag of this isochrone. Top middle: proper motion of Boo1 candidate member stars selected using proper-motion and isochrone cuts. Top right: stars that pass the isochrone cut but not the proper-motion cut. The proper motion of Boo1 is shown as a triangle. Bottom: spatial distribution of all stars in our original catalog (left), stars that pass the isochrone cut (middle), and stars that pass the isochrone and proper-motion cut (right) centered at the position of Boo1.

3.3.1. Deriving Photometric Metallicities

To illustrate how we compute metallicity from photometry, we present a grid in Figure 4 that shows $u - g - 0.9 \times (g - i)$ and $g - i$ colors separated by four different surface gravities, where we determine the surface gravity of each star by interpolating along the same isochrone as in Section 3.1. This grid is a modified version of the grid computed by A. Chiti et al. (2020), with the DECam u-band filter used to generate synthetic photometry as opposed to the SkyMapper v filter in that study. The general trend of the grid shows that metallicity decreases as the $u - g$ color and $g - i$ color become bluer at a fixed surface gravity. The data points of each star are located in this parameter space for a given surface gravity based on their dereddened DECam u-, g-, and i-band magnitudes. We interpolate the metallicity of each star using this grid.

Note that we adjust the synthetic u-band magnitudes down by 0.07 mag to better match our photometric metallicities with spectroscopic metallicities in the literature. This shift is roughly consistent with the shift applied in A. Chiti et al. (2020) to their synthetic SkyMapper v magnitudes, which is an empirically driven correction that accounts for the difference between photometric and spectroscopic metallicities due to potential imperfections in the grid of synthetic spectra.

We note also that the photometric metallicities derived for nonmember stars in our catalog are inaccurate because these stars are not located at the distance of the system and have different surface gravity values than member stars on the red giant branch. We do not apply any metallicity corrections to obtain accurate values for the nonmember stars in our catalogs, as an accurate distance measurement is required to derive their surface gravity. An upper limit on the effect of surface gravity on photometric metallicities, in cases of large distance errors for nonmembers, is the metallicity difference caused by dwarf-giant misclassification. This difference is up to 0.4 dex in our model using u-band photometry, so the metallicity error due to large distance uncertainties should not exceed this range. However, we note that we do extend the stellar parameter range of the MSTO grid of synthetic spectra in A. Chiti et al. (2020) to include main-sequence stars ($3.5 < \log g \leqslant 5$) and compute synthetic photometry for those. This main-sequence grid is later used to adjust for the photometric metallicity difference when the star is assumed to be on the red giant branch as opposed to the main sequence in Section 4.1.3 when we estimate the contamination rate due to MW foreground main-sequence stars using the Besançon model.

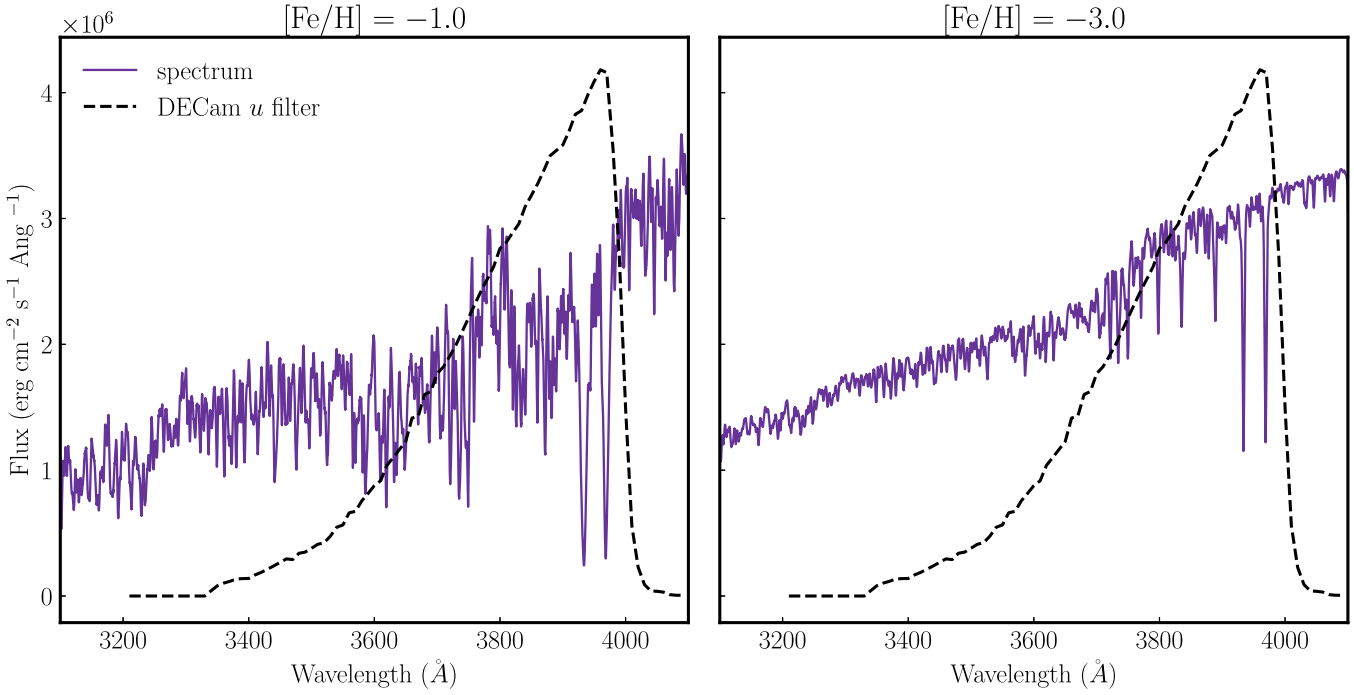

Figure 3. An illustration of why the DECam u-band is sensitive to metallicity. Left: a synthetic spectrum generated by `Turbospectrum` (R. Alvarez & B. Plez 1998; B. Plez 2012) for a sample cool red giant star with metallicity [Fe/H] = −1 overlaid with the bandpass of the DECam u filter. Right: the synthetic spectrum for a sample star with the same surface gravity and surface temperature but with metallicity [Fe/H] = −3. The Ca II K metal absorption lines are more prominent for more metal-rich stars (left), and the DECam u-band filter completely covers this feature. Therefore, the more metal-rich a star is, the dimmer it appears in the DECam u band. This correlation provides a way to associate the DECam u-band magnitude of a star with its metallicity, as shown in Figure 4.

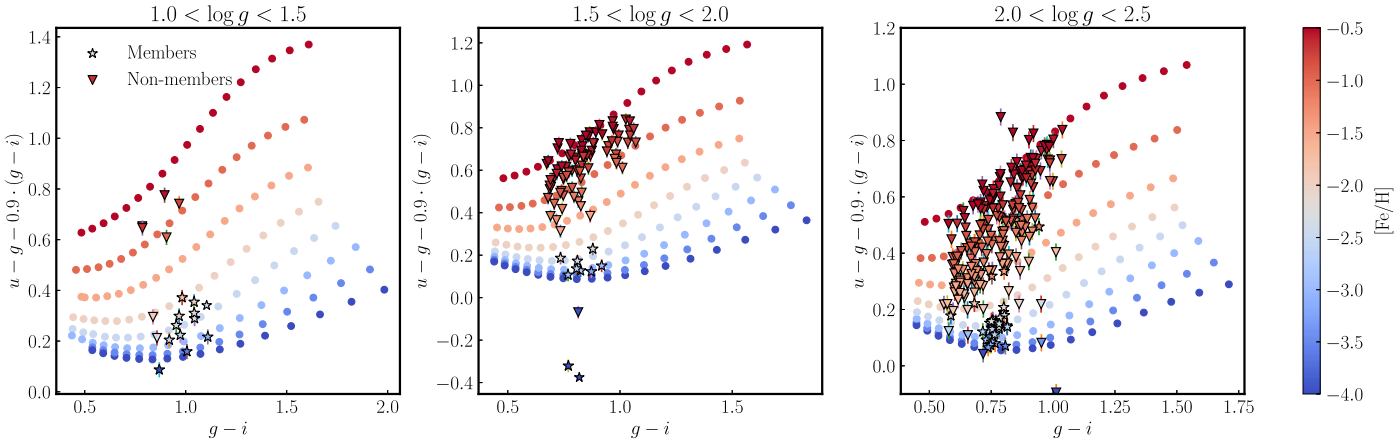

Figure 4. The relation $u - g - 0.9 \times (g - i)$ as a function of $g - i$ color for three different surface gravity bins, color coded by metallicity [Fe/H]. We manually shift the iso-metallicity lines down by 0.07 to match our photometric metallicity with spectroscopic results (Section 3.3.1). Stars (triangles) are selected candidate member stars (nonmember stars) that pass (do not pass) our isochrone, proper-motion, and metallicity cuts. In general, the grid shows that, for stars with surface gravity $\log g = 1$, 2, a higher $g - i$ color is associated with a higher $u - g - 0.9 \times (g - i)$ value, and stars with a higher metallicity tends to have higher $u - g - 0.9 \times (g - i)$ values. The $u - g - 0.9 \times (g - i)$ vs. $g - i$ parameter space cleanly separates metal-poor stars from metal-rich ones.

The metallicity distribution of candidate member and nonmember stars is shown in Figure 5, where candidate member stars are defined as those that pass our proper-motion and isochrone cuts in Section 3.1 and Section 3.2, while nonmember stars are defined as those that pass the isochrone cut but not the proper-motion cut. We observe that candidate member stars have significantly lower metallicities than nonmember MW foreground stars, indicating the accuracy of our photometric metallicities. We further apply a metallicity cut of [Fe/H] $\leqslant -1.5$ to select metal-poor candidate member stars. We choose -1.5 to ensure both a more complete and pure sample, and we discuss the details in Section 4.1.3.

However, there are some nonmember stars in the low-metallicity regime. By plotting their photometric locations in $u - g - 0.9 \times (g - i)$ versus $g - i$ colors, we found that they are typically located out of range of the iso-metallicity lines in Figure 5 and thereby off-grid relative to our synthetic photometry, indicating that their photometric metallicity is likely inaccurate.

3.3.2. Validating Photometric Metallicities

To assess the accuracy of our photometric metallicity calculation, we compare the photometric metallicities of our

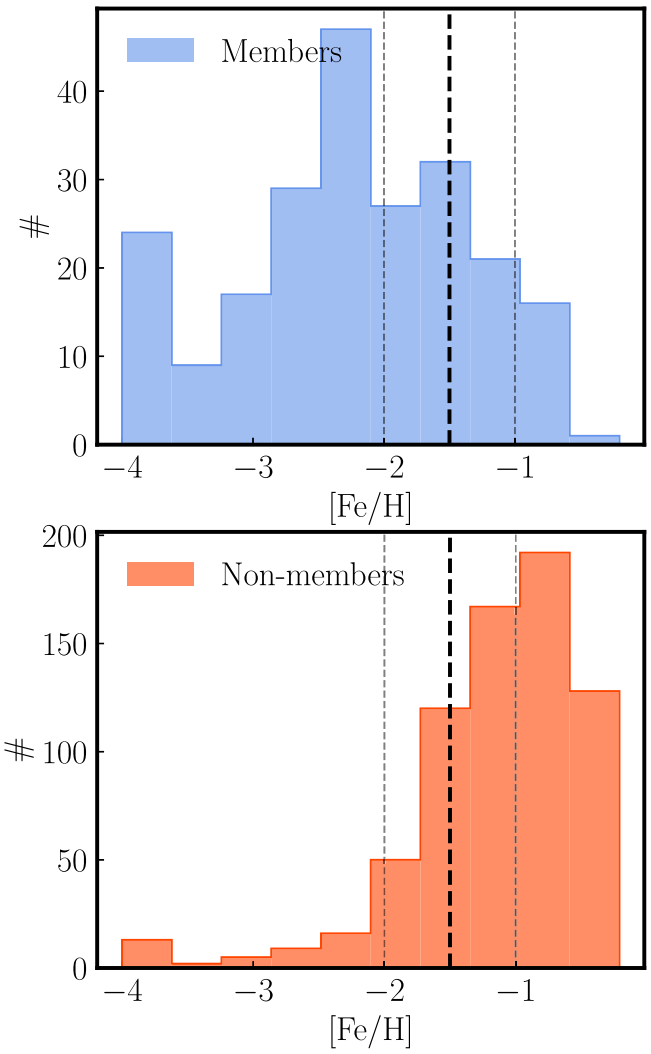

Figure 5. The distribution of photometric metallicity for candidate member (blue) and nonmember stars of Boo1 (orange). It is evident that the two groups are clearly distinguished by their metallicity, with candidate member stars having low metallicity ([Fe/H] $\leqslant -1.5$) and nonmembers having high metallicity ([Fe/H] $\geqslant -1.5$). However, it should be noted that some nonmember stars appear in the low-metallicity range. In Section 3.3, we discuss that this might be due to those nonmember stars being off-grid in the parameter space shown in Figure 4, and the photometric metallicity calculation is inaccurate for off-grid stars. Such off-grid stars can be seen in the buildup at [Fe/H] $= -4.0$ in both histograms.

candidate member stars with the spectroscopic metallicities from S. A. Jenkins et al. (2021) and A. Frebel et al. (2014) for Boo1 and Seg1, respectively. The error of our photometric metallicities is the quadratic sum of the systematic uncertainty of our method (0.17 dex, taken from analysis with the same grid from A. Chiti et al. 2020) and the error propagated from the photometric uncertainty. The right two panels of Figure 6 show that the mean offset of the two metallicities is small for both Boo1 and Seg1 stars, with $1\sigma \lesssim 0.2$ dex.

There are three outliers from the one-to-one line in the Boo1 sample (open circles), which we find out to be outliers in the $u - g - 0.9(g - i)$ versus $g - i$ grid and thus have biased low photometric metallicities and higher photometric metallicity errors as can be seen in the middle panel of Figure 6. The synthetic grid in Figure 4 shows that iso-metallicity lines are more tightly clustered at lower metallicity, so a u-band uncertainty would translate to a larger photometric metallicity uncertainty at lower metallicity. Thus, low-metallicity outliers with correspondingly larger uncertainties are more likely to appear than metal-rich outliers at the lowest metallicities, potentially explaining why the three outliers all have photometric metallicities lower than spectroscopic metallicities. Nevertheless, for our purposes, the three outliers do not affect our sample because they pass our metallicity cut and are members. Our goal of this study is to select potential members using photometric metallicities, as opposed to characterizing the metallicity distribution of the UFD. Note that the outlier in the Seg1 comparison (right panel of Figure 6) at $[\mathrm{Fe/H}]_{\mathrm{phot}} \approx -2$ is Segue 1-7 (J. E. Norris et al. 2010), an extremely carbon-enhanced star with [C/Fe] $= 2.3$ at [Fe/H] $= -3.57$ (A. Frebel et al. 2014). These stars are known to have photometric metallicities biased high due to the CN feature at ~3800 Å (E. Starkenburg et al. 2017).

4. Candidate Member Star Catalog and Member Star Validation

In previous sections, we demonstrate that we can effectively select candidate member stars in the peripheries of UFDs using photometric metallicities from DECam u band. In this section, we show the spatial distribution of detected candidate member stars for Boo1, Boo2, and Seg1. To gain a statistical understanding of our sample, we calculate the purity (defined as the ratio of the number of our selected candidate member stars that are actually members in the combined catalog to the total number of our selected candidate member stars) and completeness of our selected candidate member stars for all three systems using the Besançon model of stellar population synthesis of the Galaxy (A. C. Robin et al. 2003; M. A. Czekaj et al. 2014)[9] and literature samples of members. We also discuss the implications of the candidate member star spatial distribution considering their proper motions. Finally, for each identified star, we calculate an estimate of purity and use this as a measure to guide future spectroscopic follow-up.

4.1. Boo1

4.1.1. Spatial Distribution of Boo1 Candidate Members

In Figure 7, we present the spatial distribution of candidate member stars in Boo1 that satisfy our isochrone, proper-motion, and metallicity cuts as described in Section 3. For stars with $m_g < 20$, we observe that the majority of them form an inclined streak that aligns with the proper motion of most stars. This echoes suggestions in the literature that Boo1 is currently experiencing tidal disruption by the MW (N. Longeard et al. 2022; A. B. Pace et al. 2022). Moreover, we identify several new candidate member stars located at distances of ~3–5 half-light radii from the center.

In Figure 8, we compare the spatial distribution of our selected candidate member stars to that of member and nonmember stars in the S. A. Jenkins et al. (2021) and N. Longeard et al. (2022) catalogs. We apply our isochrone and proper-motion selections to determine members/nonmembers in the two catalogs to enable a fair comparison. For stars with $m_g < 19.5$, we identify more candidate member stars at large radii than in previous catalogs. We also identify more faint stars ($m_g < 20.2$) than in previous catalogs; however, some of these

[9] https://model.obs-besancon.fr/modele_home.php

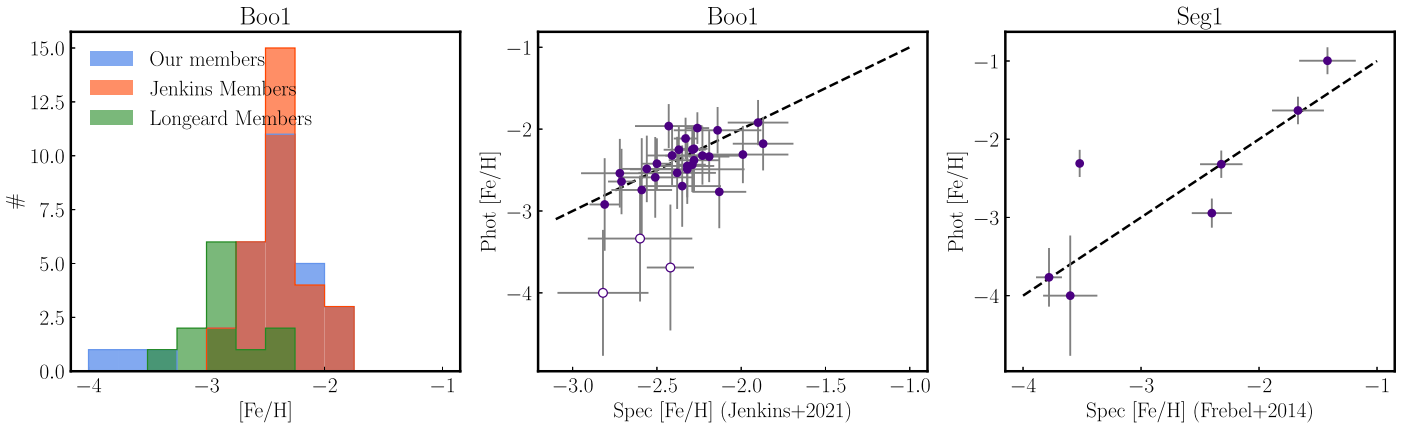

Figure 6. Left: the distribution of photometric metallicity for our selected candidate member stars (blue), member stars from S. A. Jenkins et al. (2021; red), and N. Longeard et al. (2022; green). Note that we exclude horizontal branch stars in our analysis, and stars from our catalog and from the Jenkins et al. catalog are of the same magnitude range ($m_g < 21.5$). Middle: the photometric metallicities obtained for Boo1 stars in this work are compared with the metallicities obtained by S. A. Jenkins et al. (2021) for the same sample of stars. Our error includes both the systematic uncertainty of our calculation method (0.17 dex) and the uncertainty propagated from the photometric uncertainty. The points follow a clean one-to-one relationship with a 1σ scatter < 0.2 dex, except for three stars in the bottom left (open circles). See discussion in Section 3.3.2 on these stars. Right: comparison between our photometric metallicities and spectroscopic metallicities from A. Frebel et al. (2014) of Seg1 stars. The points also follow a clean one-to-one relationship with minimal scatter, further validating the accuracy of our photometric metallicity calculation apart from one outlier. Note that the outlier (at $[\mathrm{Fe/H}]_{\mathrm{phot}} \approx -2$) is Segue 1-7 (J. E. Norris et al. 2010), an extremely carbon-enhanced star with $[\mathrm{C/Fe}] = 2.3$ at $[\mathrm{Fe/H}] = -3.57$ (A. Frebel et al. 2014).

stars may be nonmembers with large proper-motion uncertainty, allowing them to pass the proper-motion cut, or MW foreground stars with low metallicity. The contamination rate increases as we consider fainter magnitudes (e.g., $m_g > 20.5$), but for our sample of stars with $m_g < 20.2$ we still retain an elongated feature for the candidate stars within $5r_e$ in the lower-left panel of Figure 8. We fit a two-dimensional Gaussian to the distribution of stars with $m_g < 20.2$ and obtain an elliptical fit with a best-fit ellipticity of 0.406 ± 0.014 and a position angle of $2\overset{\circ}{.}35 \pm 1\overset{\circ}{.}05$, which is consistent within 1σ of the systematic values in Table 2.

4.1.2. Completeness of Boo1 Sample

We now calculate the completeness of our selected star sample, which is an essential metric for assessing the accuracy of our candidate member star selection. Boo1 is a particularly suitable target for this analysis, as it is the only MW UFD that has an extensive sample of literature member stars in this study. By quantifying the completeness and purity of our selection of candidate Boo1 members, we can obtain a preliminary estimate of the potential bias and uncertainty in our selection criteria, which could be applied to other systems in this study.

The completeness of our selected sample of candidate member stars for Boo1 is determined by calculating the ratio of the number of stars in our catalog that are also present in the combined S. A. Jenkins et al. (2021) and N. Longeard et al. (2022) catalog to the total number of stars in the combined catalog. To compute this, we first cross-match the two catalogs, which yields a total of 48 member stars. Subsequently, we cross-match these 48 catalog member stars with our selected stars in Section 3 that satisfy the metallicity cuts $[\mathrm{Fe/H}] < -1$, $[\mathrm{Fe/H}] < -1.5$, and $[\mathrm{Fe/H}] < -2$. We obtain 47, 45, and 42 overlaps, respectively. Hence, the completeness rates are 97.9%, 93.8%, and 87.5%, respectively. These results indicate that lower-metallicity cuts may exclude more true members. Note that we only consider red giant branch stars here and exclude horizontal branch stars.

4.1.3. Purity of Boo1 Sample

Purity is defined as the ratio of the number of our selected candidate member stars that are actually members in the combined catalog to the total number of our selected candidate member stars. We first combine all the stars (members and nonmembers) in the S. A. Jenkins et al. (2021) and N. Longeard et al. (2022) catalogs. Next, we cross-match these stars with our selected stars that pass the isochrone, proper-motion, and metallicity cuts $[\mathrm{Fe/H}] < -1$, $[\mathrm{Fe/H}] < -1.5$, and $[\mathrm{Fe/H}] < -2$ to obtain three different samples. We compute the purity rate for different metallicity cuts using these overlaps.

As we only have two catalogs available to compute the completeness and purity rates, and only the N. Longeard et al. (2022) catalog extends beyond 1 half-light radius of Boo1, we require an independent method to estimate the contamination rate from MW foreground stars. We use the Besançon model, which enables us to simulate the number of MW foreground stars within 5 half-light radii from Boo1. We adopt the SDSS +JHK photometric system in our simulations, and our field of view encompasses 150 kpc, with the frame centered on Boo1 and a solid angle of 100 deg^2. We use the large field instead of the small field (10 deg^2) since the small field contains only a few foreground stars that satisfy our selection criteria, leading to a biased estimate of the foreground contamination rate, particularly at larger radii. We verified that the proper-motion and radial-velocity distributions do not show spatial variations in the 100 deg^2 field that was selected.

We select all stars with g-band magnitudes between $g = 16$ and $g = 23$ and generate model stars without applying a proper-motion error function in the query. We use the correlation between proper-motion uncertainties and the dereddened g-band magnitudes in our sample of observed nonmembers and fit an exponential function $0.01 + e^{1.2 \cdot m_g - 25}$, and use this to derive the proper-motion error for simulated stars. The model generates a total of 311,416 stars, and we apply our isochrone, proper-motion, and metallicity $[\mathrm{Fe/H}] < -1.5$ cuts to obtain 1712 stars that pass all our selection criteria. Since most of the MW foreground stars are main-sequence stars, their metallicities will be inaccurate if we use the synthetic photometry grid

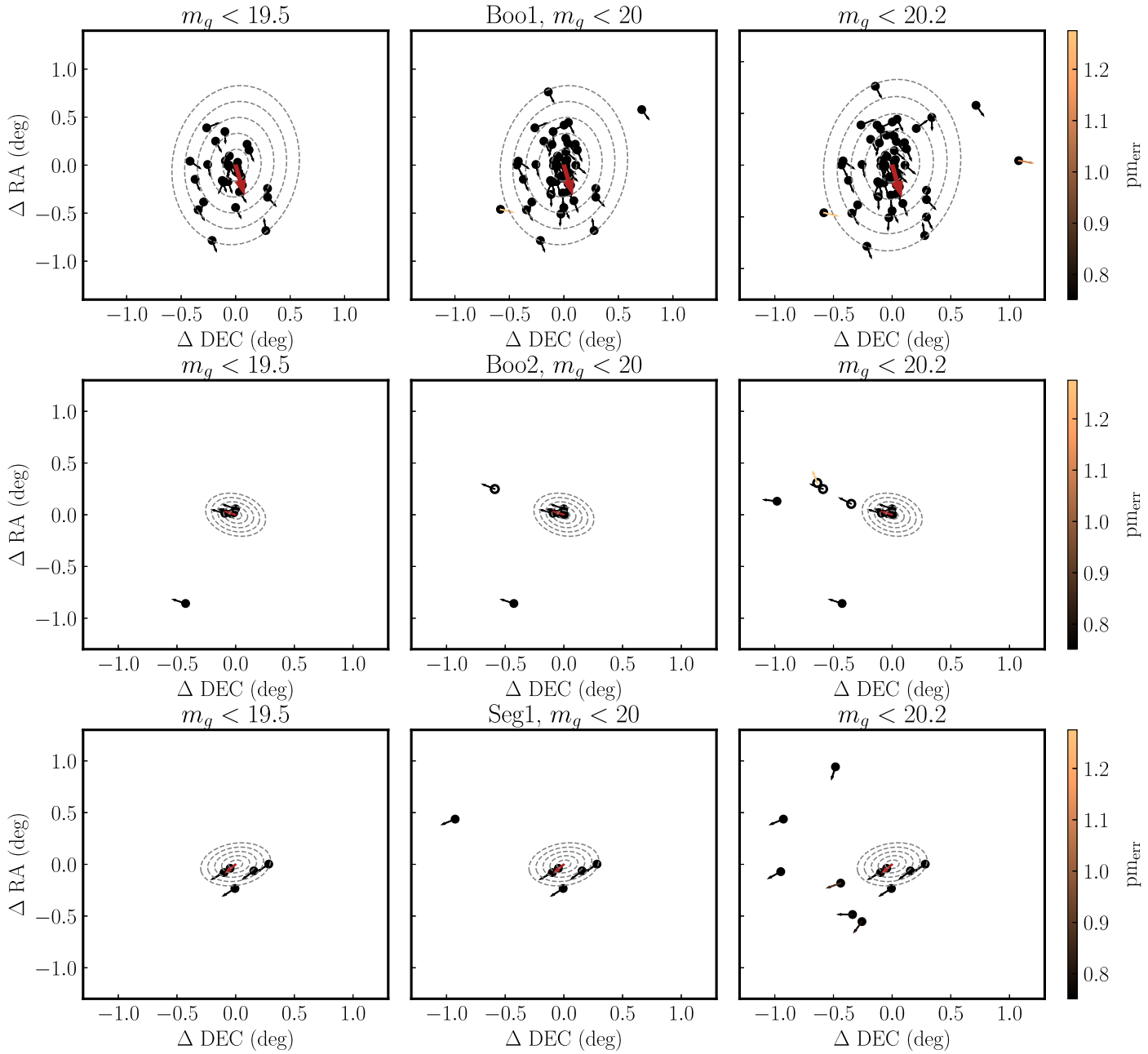

Figure 7. Spatial distribution of candidate member stars in our catalog for Boo1 (top), Boo2 (middle), and Seg1 (bottom). We divide the candidate member stars by three magnitudes: $M_g < 19.5$ (left), $M_g < 20$ (middle), and $M_g < 20.2$ (right). The dashed gray ellipses denote 1, 2, 3, 4, and 5 half-light radii of each system with ellipticity and position angle listed as in Table 2. Each arrow represents the reflex-corrected velocity vector of a star calculated from its proper motion, and the red arrow indicates the systemic reflex-corrected velocity vector from Table 2. For Boo1 (top), our candidate member star population extends beyond ~$5r_h$, and they form a streak in the same direction as the proper motion of the system in the brightest sample (top-left panel), indicating possible tidal disruption. For Boo2 (middle rows), most of our candidate member stars lie within $2r_h$. There exists an extension of stars northeast of the system, but three of them (open black circles) are outliers in the CMD, indicating they may not be members. The other two solid black points outside $5r_h$ could be targets for future spectroscopic follow-up. For Seg1 (bottom), we apply an additional cut of [Fe/H] < -2 to weed out potential 300S member stars (Section 4.2.1). There is also a handful of candidates southeast of the system, in addition to potential contamination from the Sagittarius stream or other substructures (Section 4.2.1).

obtained for giant stars in Section 3.3.1. To get accurate metallicities for the MW foreground stars, we use the synthetic photometry grid described in Section 3.3.1 for main-sequence stars ($3.5 < \log g \leqslant 5.0$). From this grid, we derive the metallicity differential between assuming a star is on the main sequence versus the red giant branch as a function of the star's uncorrected metallicity and SDSS $g - r$ color. We apply this correction to the main-sequence stars in the Besançon catalog to mimic how their metallicities would appear in our analysis. We further apply a magnitude cut $m_g < 21.5$, as all our candidate member stars have $m_g < 21.5$.

We assume a uniform spatial *density* distribution of MW foreground stars and calculate the MW contamination rate as the total number of stars that pass all our selection criteria (1712) divided by the total FOV (100 deg^2). We divide the area into several radial bins: 0–1 r_h, 1–2 r_h, 2–3 r_h, 3–4 r_h, etc., and for each bin the estimated MW contamination number is the area of the annulus times the contamination rate. For

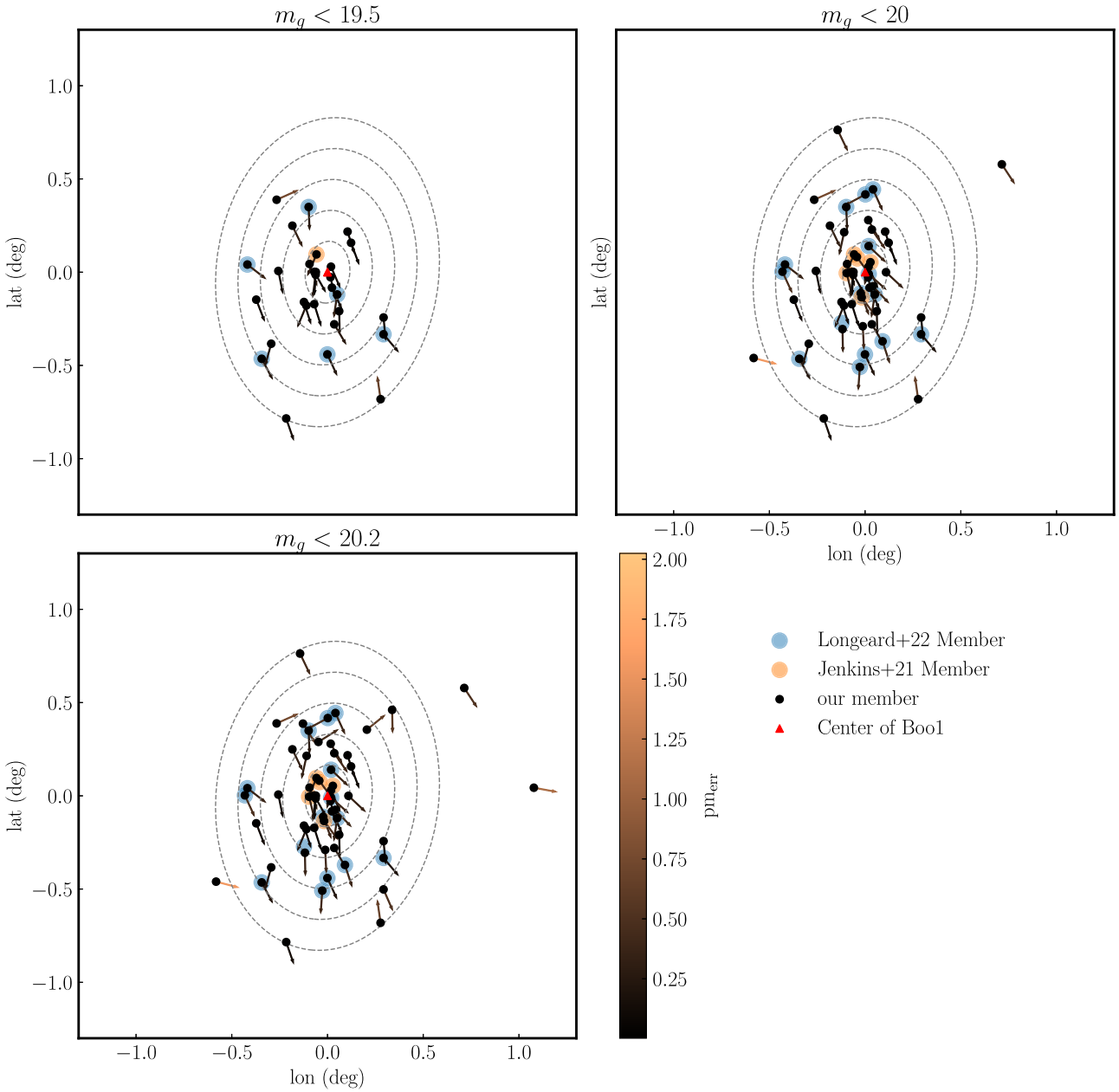

Figure 8. Spatial distribution of candidate member stars for Boo1 with a metallicity cut [Fe/H] < -1.5 compared with member stars in N. Longeard et al. (2022; blue) and S. A. Jenkins et al. (2021; orange). Other symbols are the same as in Figure 7. Most of the member stars in the Jenkins et al. catalog are located within 1 half-light radius, while the member stars in the Longeard et al. catalog extend out to approximately 3 to 4 half-light radii for stars brighter than $m_g = 20.2$. We were able to recover all of the member stars in the Jenkins et al. and Longeard et al. catalogs except for one that has a photometric metallicity of -1.47 and thus does not pass our -1.5 photometric metallicity cut. We discuss the completeness and purity of our selected candidate member star sample compared to the combined Jenkins et al. and Longeard et al. catalog in Section 4.1.2.

each annulus, we further divide it into magnitude bins $m_g = (16, 19.5, 20, 20.5, 21, 21.5)$. We record the number of candidate member stars and MW foreground stars that fall into each radial and magnitude bin. Then, the purity of each star in a specific radial and magnitude bin is computed as (# of candidate members − # MW foreground)/(# of candidate members) in that bin. Stars that fall into the same radial and magnitude bin will have the same purity. We use purity as a guide for spectroscopic studies to decide which stars should be targets given limited telescope time.

As shown in Figure 9, both the number of candidate member stars and the number of MW foreground stars increase from bright to faint magnitudes. From small to large radial distances, the number of candidate member stars decreases significantly and the number of foreground stars increases steadily. Going from metallicity cut [Fe/H] < -1 to [Fe/H] < -1.5 decreases the foreground number with minimal decrease of candidate member stars, so to maximize both completeness and purity, we have chosen the metallicity cut [Fe/H] < -1.5 and apply this metallicity cut on all subsequent analyses.

We fit a function to the number of foreground stars for each system, as a function of both radius and g-band magnitude, and display the color-mesh interpolator in Figure 10. The number of MW foreground stars increases as the magnitude becomes fainter and the radius grows larger. For Boo1, at a g-band magnitude of approximately 21 and a radius of around 0.°2,

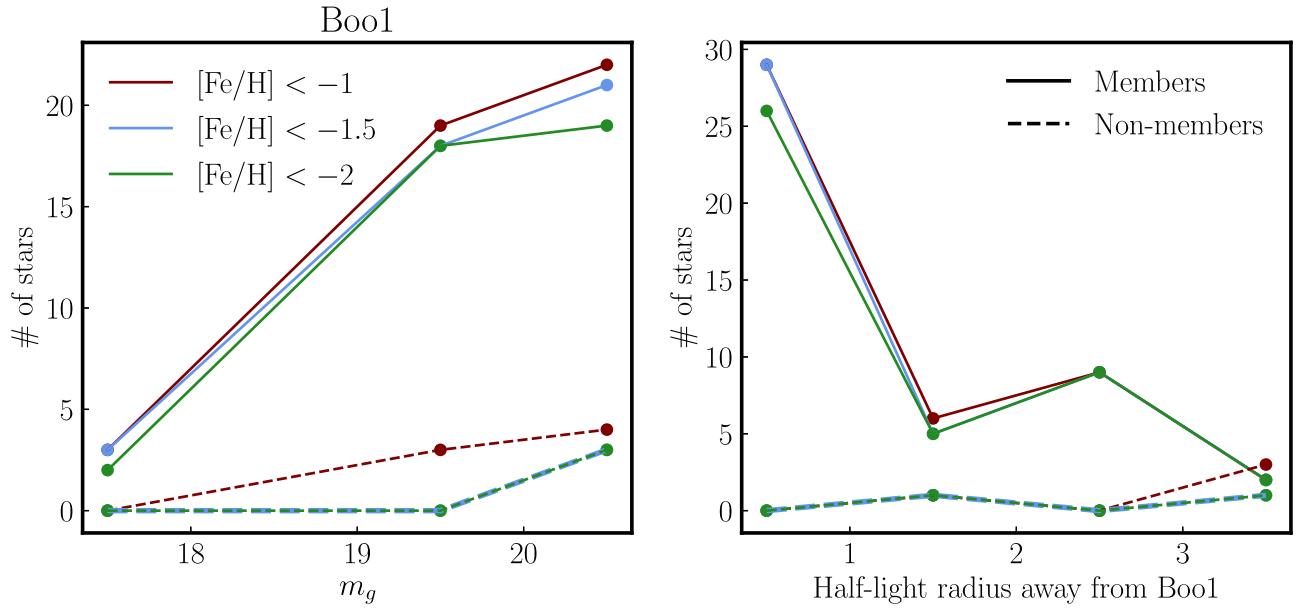

Figure 9. Number of member and nonmember stars as a function of m_g and half-light radius r_h from the center for three different metallicity cuts. Stricter metallicity cuts result in a decrease of both candidate member stars and nonmember stars. Looser metallicity cuts result in an increase in both candidate member stars and nonmember stars. As discussed in Section 4.1.3, we choose [Fe/H] < -1.5 as our final photometric metallicity cut given joint completeness and purity considerations.

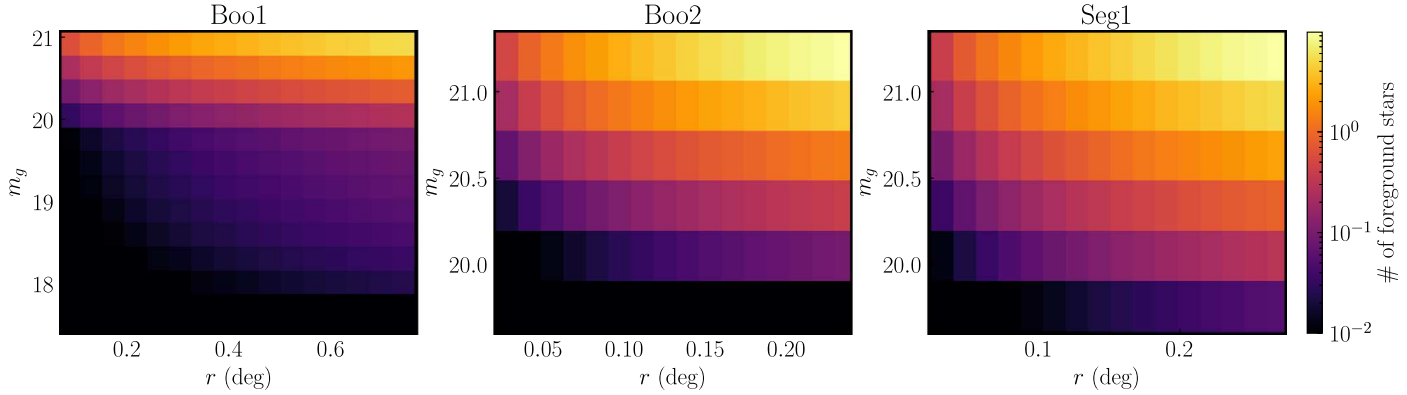

Figure 10. A 2D histogram displaying the estimated number of MW foreground stars for Boo1, Boo2, and Seg1 as a function of radius (in degrees) and m_g. The number of MW foreground stars increases as the magnitude becomes fainter and the radius grows larger.

approximately 10 foreground stars pass all of our cuts, potentially contaminating our sample.

To ensure the robustness of our method, we perform one final check by incorporating the uncertainty in metallicity into our foreground contamination estimate. We use the same sample of large-field model stars as in Section 4.1.3, where we calculated the theoretical purity rate. We fit an exponential function of the form $y = 0.0001 + e^{1.08x-25}$ to the metallicity error and g-band magnitude of our sample of nonmember stars. We then use this fitted function to get the metallicity error (y) of model stars based on their g-band magnitudes (x). Assuming a Gaussian distribution of metallicity for each model star with a mean equal to the metallicity returned by the model and a standard deviation equal to the metallicity error we calculated using the fit, we generate 1000 ensembles for each star and run 1000 simulation experiments to estimate, on average, how many stars pass all selection cuts. The standard deviation of the number of stars passing all selection cuts for the 1000 runs is approximately 2.5, indicating that there will be a variation of only around 2.5 stars passing all selection cuts if we include the metallicity uncertainty. This demonstrates that our selection is robust against metallicity uncertainties.

4.2. Boo2 and Seg1

4.2.1. Spatial Distribution

In Figure 7, we present the spatial distribution of candidate member stars in Boo2 that satisfy our isochrone, proper-motion, and metallicity cuts. Most of our identified stars with $m_g < 20$ lie within $2r_h$ of the system. For the sample brighter than $m_g = 20.2$, we detect four stars with consistent proper motions in the DECam FOV northeast of the system at large radial distances. Three of them, indicated by hollow circles in Figure 7, appear as outliers on the CMD despite passing our selection, so we flag them as unlikely members. The remaining candidate is a potential target for future spectroscopic follow-up studies.

In Figure 12, we compare the spatial distribution of our selected candidate member stars of Boo2 to that of member and nonmember stars in the A. Koch et al. (2009), A. P. Ji et al. (2016), and J. Bruce et al. (2023) catalogs. We apply our

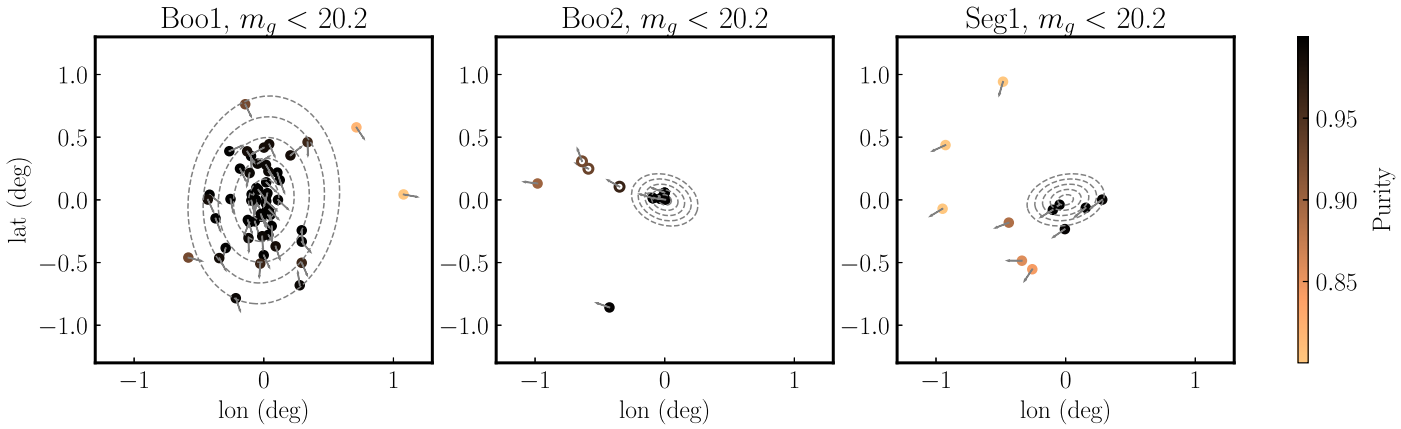

Figure 11. The spatial distribution of Boo1, Boo2, and Seg1 candidate member stars brighter than $m_g = 20.2$ color coded according to their purity. Purity decreases as the radius increases and magnitude becomes fainter. We use purity as a measure to guide future spectroscopic follow-up of the newly found potential member stars.

isochrone and proper-motion cuts to all members in the three catalogs to enable a fair comparison. Note that Boo2 has a relatively small size, but we show the entire DECam FOV (~3 deg^2) for the faint sample with $m_g < 20.2$ to include all detected candidate member stars in the DECam FOV. The four stars northeast of the system are not detected in any previous spectroscopic studies.

For Seg1, Figure 7 shows that, similar to Boo1, the spatial distribution of several new candidates in Seg1 suggests an elongation consistent with the direction of the proper motion. This may indicate signs of Seg1 undergoing tidal disruption by the MW, but further kinematic studies of distant members are needed to fully ascertain the dynamical state of the system. By comparing with the J. D. Simon et al. (2011) and A. Frebel et al. (2014) samples in Figure 13, we find a handful more candidate member stars outside of $5r_h$ to the south and to the east of the system in addition to several directly east and north. We note that the Sagittarius stream has an increasing presence toward the north of the field (e.g., V. Belokurov et al. 2006b; M. Geha et al. 2009) and the 300S stream passes east–west (S. W. Fu et al. 2018), suggesting some distant stars in these directions may be members of those streams.

4.2.2. Completeness and Purity

The completeness of our selected sample of candidate member stars for Boo2 and Seg1 is determined in the same way as in Section 4.1.2. For Boo2, every candidate member star determined in previous spectroscopic studies is identified in our photometric sample. For Seg1, to compare with J. D. Simon et al. (2011) and A. Frebel et al. (2014) catalogs, we weed out potential 300S stream members in the field of view (S. W. Fu et al. 2018) by applying an additional metallicity cut of [Fe/H] < -2 (T. S. Li et al. 2022; S. A. Usman et al. 2024). This cut also removes all Sagittarius stream members apart from its faint component (G. Limberg et al. 2023). Two member stars of Seg1, SDSS J100714+160154 and SDSS J100710+160623 (A. Frebel et al. 2014), in the two catalogs that have unusually high spectroscopic metallicities of -1.42 and -1.67, respectively, and photometric metallicities -1.00 and -1.63, do not show up in our catalog because they do not pass our [Fe/H] < -2 cut.

The purity for Boo2 and Seg1 candidate member stars is calculated in the same way as in Section 4.1.3. For Boo2, Figure 10 shows that our sample is essentially clean of contamination across all radii for stars brighter than 20.0 mag, and for Seg1 our sample is essentially clean of contamination across all radii for stars brighter than 20.0 mag. However, the region of sky around Seg1 has many substructures like the Sagittarius stream and 300S stream, so the Besançon model might underestimate the foreground contamination. Tables 4 and 5 show a representative sample of candidate member stars in our Boo2 and Seg1 catalogs, respectively, with the same columns as in Table 3.

5. Discussion

The processes that drive the formation and evolution of UFDs, including the prominence of early dwarf–dwarf mergers, the influence of supernova feedback, and the strength of tidal disruption by a massive host, are still relatively poorly constrained. Observationally, these phenomena manifest in the outskirts of these galaxies (beyond $4r_h$), which can be probed through detailed studies of their resolved stellar populations at large distances. Observational efforts have concentrated on the outskirts of the MW UFDs to identify distant member stars. This approach has unveiled extended stellar populations in many UFDs. For example, RR Lyrae (RRL) stars outside of the tidal radius of 14 UFDs (Boötes I, Boötes III, Sagittarius II, Pegasus IV, Reticulum III, Eridanus II, Eridanus III, DELVE 2, Tucana II, Tucana III, Tucana IV, Hercules, Grus II, and Ursa Major I) have been identified (C. Garling et al. 2018; A. K. Vivas et al. 2020; E. A. Tau et al. 2024). A. Chiti et al. (2021) showed that there are member stars of Tucana II out to distances of ~1 kpc, and C. Filion & R. F. G. Wyse (2021), N. Longeard et al. (2022, 2023), and X. Ou et al. (2024) have shown similar distant members and candidates in Hercules and Boötes I. J. Jensen et al. (2024) find evidence for low-density outer profiles in nine dwarf galaxies, and C.E. Martínez-Vázquez et al. (2021) reported an RRL star at $6r_h$ and another blue horizontal branch star at $>9r_h$ in Centaurus I. Here, we report multiple new bright candidate member stars ($m_g < 20.2$) of Boo1 located at $>4r_h$, five candidate member stars of Boo2 located at $>5r_h$ (including one promising candidate member), and two candidate member stars of Seg1 at $>5r_h$. These are interesting targets for spectroscopic follow-up.

Current observations strongly support the conclusion that UFDs host stars at large distances; however, the physical mechanism that relocates stars from these low-mass systems to large distances is currently uncertain. One explanation is tidal

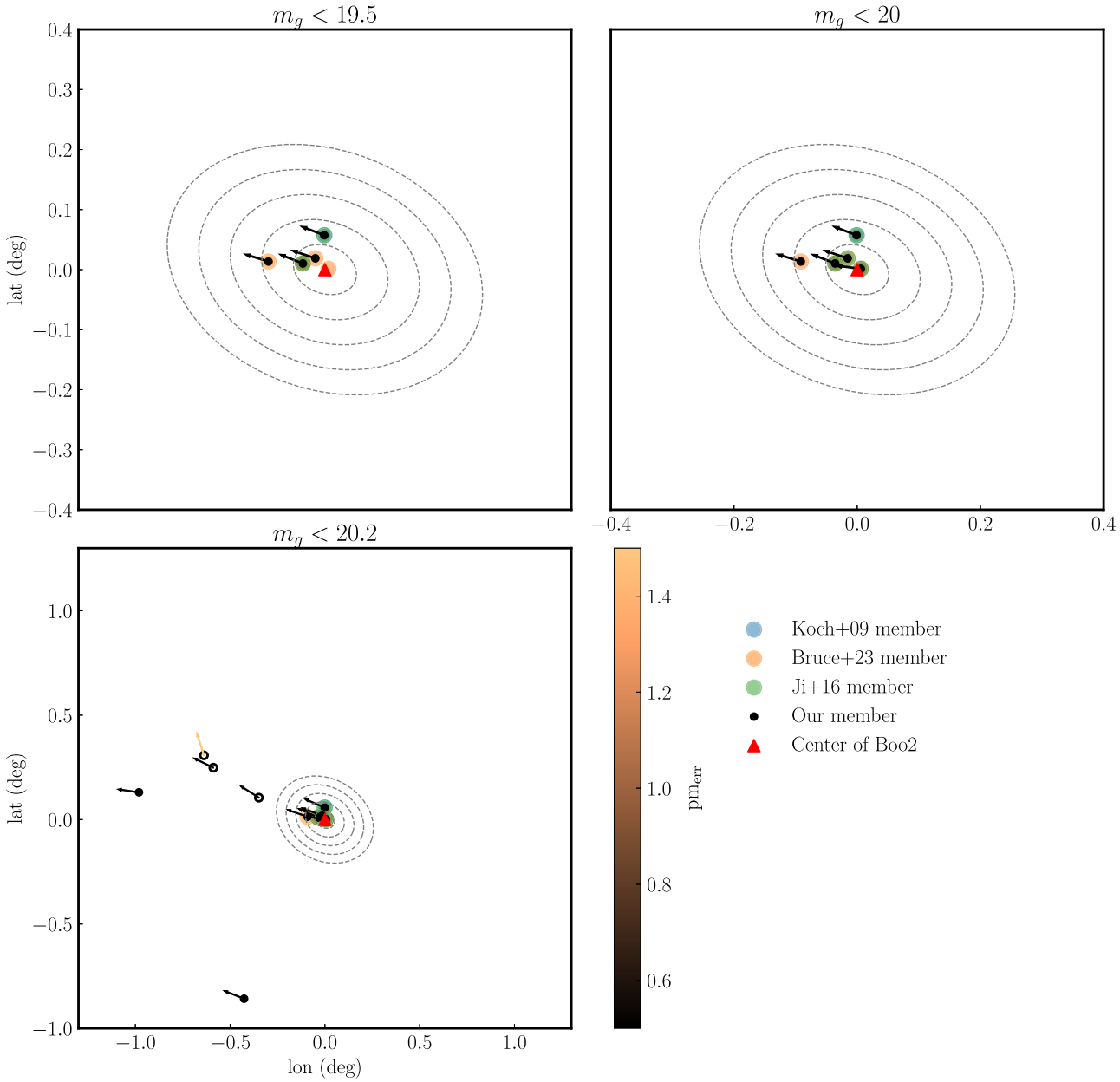

Figure 12. Spatial distribution of candidate member stars for Boo2 with a metallicity cut [Fe/H] < -1.5 compared with member stars in A. Koch et al. (2009; blue), J. Bruce et al. (2023; orange), and A. P. Ji et al. (2016; green). Other symbols are the same as in Figure 7. We recover all the member stars in all three catalogs, reaching a 100% completeness rate. For stars with $m_g < 20.2$ (lower left), we zoom out to show the entire DECam FOV (~4 deg^2). There is a hint of metal-poor candidate member stars to the south and to the east of the system, two of which (solid circles) are not outliers in CMD and thus could be interesting targets for future spectroscopic follow-up.

disruption, which transports stars to large radii through interactions with an external, more massive galaxy. Indeed, a number of studies have found evidence or have suggested that some UFDs are undergoing tidal disruption by the MW (e.g., A. Drlica-Wagner et al. 2015; J. D. Simon et al. 2017; T. S. Li et al. 2018; B. Mutlu-Pakdil et al. 2019; X. Ou et al. 2024). In particular, the previously known orientation of distant members in Boo1 and its velocity gradient strongly suggest the system is undergoing tidal disruption (C. Filion & R. F. G. Wyse 2021; N. Longeard et al. 2022; A. B. Pace et al. 2022). This is consistent with our finding of a larger number of candidates in Boo1 at large distances. The orbital parameters of Boo1, such as a comparison of half-light radius and tidal radius from modeling (i.e., Figures 5 and 6 in A. B. Pace et al. 2022), also indicate Boo1 as potentially being tidally disrupted, although it has a pericenter of ~38 kpc. For Seg1, it is less clear if MW tidal disruption is at play (see, e.g., Section 5.6 of J. Jensen et al. 2024 for a detailed discussion), even if it has a close pericenter of ~20 kpc (A. B. Pace et al. 2022). In particular, the intersection of many stellar streams with the Seg1 field makes a conclusive statement difficult. Our discovery of a few brighter ($g < 20.2$) candidate stars beyond $9r_h$ is suggestive, but not conclusive, evidence of tidal features, and spectroscopic follow-up of these stars will be important to confirm any association and interpret the nature of this system. Boo2 has a pericenter of ~36 kpc, and other orbital parameters do not show evidence of it being especially prone to tidal disruption (A. B. Pace et al. 2022).

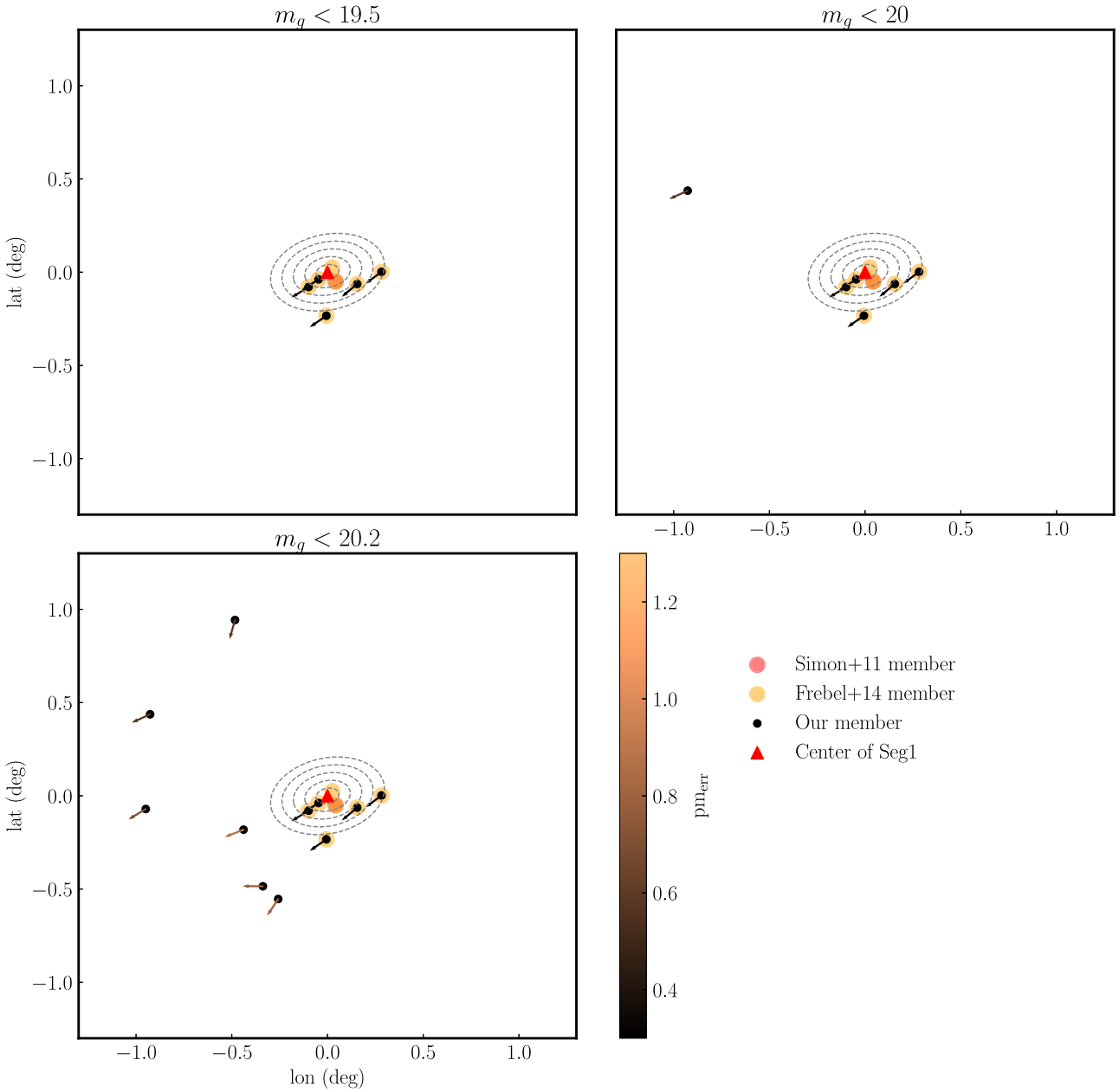

Figure 13. Spatial distribution of candidate member stars for Seg1 with a metallicity cut [Fe/H] < -2 compared with member stars in J. D. Simon et al. (2011; red) and A. Frebel et al. (2014; orange). We recover all but two member stars in the two catalogs, SDSS J100714+160154 and SDSS J100710+160623, which have unusually high spectroscopic metallicities of -1.42 and -1.67, respectively (A. Frebel et al. 2014), and photometric metallicities -1.00 and -1.63, so they are cut off from our photometric metallicity cut of [Fe/H] $= -2$. We find a handful more candidate members to the south of the system compared to previous studies, in addition to a few east and north. As discussed in Sections 4.2.1 and 4.2.2, the presence of the 300S and Sagittarius streams in the field of view may affect the purity of these candidates.

Another plausible mechanism to displace stars to large distances relies on processes during the formation of UFDs, such as early galaxy mergers and stellar feedback, which may kinematically heat the system and form an extended stellar halo (A. Deason et al. 2014). For example, the extended stellar profiles of some UFDs (e.g., Tucana II; A. Chiti et al. 2021) have been discussed as a potential result of the merging of two primordial galaxies at $z \gtrsim 2$ (A. Deason et al. 2014; Y. Tarumi et al. 2021), or early supernova feedback driven by a bursty star formation history (C. Wheeler et al. 2019; Y. Pan & A. Kravtsov 2023). This is also related to claims that higher-mass dwarf spheroidals have cored dark-matter profiles due to bursty star formation or supernova outflows (e.g., A. Pontzen & F. Governato 2012; N.C. Amorisco et al. 2014; J. I. Read et al. 2016; M. D. A. Orkney et al. 2021).

While we cannot claim a clear mechanism for the formation of the stellar outskirts of UFDs from this study alone, spectroscopic follow-up of candidate members is one observational avenue to further distinguish between potential formation processes (e.g., to investigate velocity gradients and chemical differences between the central/outer populations; A. Chiti et al. 2023; F. Waller et al. 2023). We provide a list of candidate members in Tables 3, 4, and 5 to help guide such work, and also indicate stars that have already been observed by ongoing but unpublished work from the S5 Collaboration. In particular, we highlight that spectroscopic follow-up of brighter distant candidates of Boo2 or Seg1 may pin down the evolutionary nature of these systems, given that their orbital parameters suggest that they may not be especially prone to

disruption (e.g., A. B. Pace et al. 2022). If the distant stars do reflect tidal perturbations, then it may suggest that larger numbers of UFDs have potentially been tidally perturbed and lost a significant fraction of their dark-matter halo mass due to interactions with the MW (e.g., J. Peñarrubia et al. 2008).

6. Conclusions

In this paper, we show that DECam *u*-band photometry, which covers the prominent Ca II K metal absorption line, can be used to compute photometric metallicities and effectively select candidate member stars at large radial distances for three MW UFDs: Boo1, Boo2, and Seg1. We combine multiband photometry information from DELVE (A. Drlica-Wagner et al. 2022), proper-motion information from Gaia (Gaia Collaboration et al. 2023), and photometric metallicities from DECam to select candidate member stars. We present the spatial distribution of candidate member stars for all three systems. Two of the systems potentially show signs of tidal disruption, but further spectroscopic follow-up is necessary to confirm this. We assess the purity and completeness of our sample, and use purity as a measure to guide future spectroscopic follow-ups of the new candidate member stars we found. Our technique holds potential for future efforts to identify candidate member stars at large radii in other UFDs of the MW, utilizing metallicity-sensitive filters with the Legacy Survey of Space and Time (LSST) and the newly developed, narrowband Ca HK filter on DECam. Our main findings can be summarized as follows:

1 The DECam photometry can be used to efficiently distinguish between candidate member and nonmember stars and to compute photometric metallicities (Figures 4, 5). Our photometric metallicities generally agree with spectroscopic metallicities from S. A. Jenkins et al. (2021) for Boo1 member stars and from A. Frebel et al. (2014) for Seg1 member stars.
2 The spatial distribution of Boo1 shows a prominent elongation along the direction of the proper motion of the system, indicating that Boo1 is possibly undergoing tidal disruption by the MW (Figures 7 and 8). This corroborates previous wide-field spectroscopic studies of the system (e.g., N. Longeard et al. 2022).
3 The spatial distribution of Boo2 shows that there are four candidate member stars in the northeast direction of the system consistent with the proper motion of the system, but three of them turn out to be outliers in the CMD and thus may be unlikely to be members. (Figures 7 and 12). The one remaining candidate could be a target for future spectroscopic follow-up.
4 Seg1 is contaminated by the stellar streams 300S and Sagittarius, so we add an additional metallicity cut of $[\mathrm{Fe/H}] < -2$ to lessen substructure contamination. The spatial distribution of Seg1 also suggests a hint of a tidal disruption feature (Figures 7, 13), but spectroscopic follow-up is needed of identified candidate members.
5 We present tables of identified member stars and candidate members to aid future spectroscopic studies, in addition to providing a literature compilation of members. We note that several candidates already have spectroscopy from the Southern Stellar Stream Spectroscopic Survey (S^5 collaboration 2024, in preparation), and this information is also indicated in the tables.

Acknowledgments

This work is supported by the Quad Undergraduate Research program at the University of Chicago, and the Department of Astronomy and Astrophysics at the University of Chicago. We thank Sergey Koposov for providing his code for proper-motion reflex corrections. We also thank the anonymous referee for constructive feedback on an earlier version of this paper. The Proposal ID for the DECam observations is 2021A-0272.

A.C. is supported by a Brinson Prize Fellowship at the University of Chicago/KICP. A.D.W. acknowledges support from NSF grants AST-2006340, AST-2108168, and AST-2307126. A.P.J. acknowledges support from NSF grant AST-2307599. G.L. acknowledges FAPESP (procs. 2021/10429-0 and 2022/07301-5).

This work has made use of data from the European Space Agency (ESA) mission Gaia (https://www.cosmos.esa.int/gaia), processed by the Gaia Data Processing and Analysis Consortium (DPAC, https://www.cosmos.esa.int/web/gaia/dpac/consortium). Funding for the DPAC has been provided by national institutions, in particular the institutions participating in the Gaia Multilateral Agreement.

The DECam Local Volume Exploration Survey (DELVE; NOAO Proposal ID 2019A-0305, PI: Drlica-Wagner) is partially supported by Fermilab LDRD project L2019-011, the NASA Fermi Guest Investigator Program Cycle 9 No. 91201, and NSF AST-2307126.

This project used data obtained with the Dark Energy Camera (DECam), which was constructed by the Dark Energy Survey (DES) collaboration. Funding for the DES Projects has been provided by the U.S. Department of Energy, the U.S. National Science Foundation, the Ministry of Science and Education of Spain, the Science and Technology Facilities Council of the United Kingdom, the Higher Education Funding Council for England, the National Center for Supercomputing Applications at the University of Illinois at Urbana-Champaign, the Kavli Institute of Cosmological Physics at the University of Chicago, the Center for Cosmology and Astro-Particle Physics at the Ohio State University, the Mitchell Institute for Fundamental Physics and Astronomy at Texas A&M University, Financiadora de Estudos e Projetos, Fundação Carlos Chagas Filho de Amparo á Pesquisa do Estado do Rio de Janeiro, Conselho Nacional de Desenvolvimento Científico e Tecnológico and the Ministério da Ciência, Tecnologia e Inovação, the Deutsche Forschungsgemeinschaft, and the Collaborating Institutions in the Dark Energy Survey.

The Collaborating Institutions are Argonne National Laboratory, the University of California at Santa Cruz, the University of Cambridge, Centro de Investigaciones Enérgeticas, Medioambientales y Tecnológicas–Madrid, the University of Chicago, University College London, the DES-Brazil Consortium, the University of Edinburgh, the Eidgenössische Technische Hochschule (ETH) Zürich, Fermi National Accelerator Laboratory, the University of Illinois at Urbana-Champaign, the Institut de Ciències de l'Espai (IEEC/CSIC), the Institut de Física d'Altes Energies, Lawrence Berkeley National Laboratory, the Ludwig-Maximilians Universität München and the associated Excellence Cluster Universe, the University of Michigan, the National Optical Astronomy Observatory, the University of Nottingham, the Ohio State University, the OzDES Membership Consortium, the University of Pennsylvania, the University of Portsmouth, SLAC

National Accelerator Laboratory, Stanford University, the University of Sussex, and Texas A&M University.

Based in part on observations at Cerro Tololo Inter-American Observatory, National Optical Astronomy Observatory, which is operated by the Association of Universities for Research in Astronomy (AURA) under a cooperative agreement with the National Science Foundation.

Database access and other data services are hosted by the Astro Data Lab at the Community Science and Data Center (CSDC) of the National Science Foundation's National Optical Infrared Astronomy Research Laboratory, operated by the Association of Universities for Research in Astronomy (AURA) under a cooperative agreement with the National Science Foundation.

The software packages NUMPY (S. van der Walt et al. 2011), SCIPY (E. Jones et al. 2001), Astropy (Astropy Collaboration et al. 2013, 2018, 2022), MATPLOTLIB (J. D. Hunter 2007), and Github were invaluable in conducting the analyses presented in this paper. We also used the Starlink Tables Infrastructure Library Tool Set (STILTS; M. B. Taylor 2006) extensively.[10] Additionally, this research relied heavily on the Astrophysics Data Service (ADS[11]) and the preprint repository arXiv.[12]

Appendix
Member Star Flags

We use purity as a measure of how likely our identified star is a true member to guide future spectroscopic studies, and report this in our tables of candidate members (Tables 3, 4, 5). MEM_FLAG = 0 means this star is an identified member star in the literature. MEM_FLAG = 1 means this star is an identified nonmember star in the literature, but we flag it as a candidate member star in our catalog. MEM_FLAG = 2 means this star is not identified in previous studies, and we identify it as a bright candidate member star ($m_g < 20.2$). These are interesting candidates for future spectroscopic studies. MEM_FLAG = 3 means this star is not identified in previous studies, and we identify it as a candidate with lower purity due to its faintness ($m_g > 20.2$). Note that in some radial and magnitude bins, the number of predicted foreground stars exceeds the observed number of stars, so we assign a purity of 0 for these cases. In these tables, we also exclude stars that are $\gtrsim$0.05 mag from the edge of our grid of synthetic photometry, have discrepant $g - r$ versus $r - i$ colors, or have entries in the Gaia DR3 variable source catalog (L. Rimoldini et al. 2023). We additionally indicate stars that may be outliers relative to the CMD under a tighter selection but still pass our isochrone tolerance in Section 3.1 through the CMD_outlier_flag column.

In Figure 11, we show a spatial distribution of candidate member stars with $m_g < 20.2$ color coded by their purity. Most of the stars we identified have high purity >95%, and all stars have purity >80%. We propose these stars (MEM_FLAG = 2) for future spectroscopic studies. Table 3 shows a representative sample of identified candidate member stars in our catalog.

[10] http://www.starlink.ac.uk/stilts/
[11] https://ui.adsabs.harvard.edu/classic-form/
[12] https://arxiv.org/

Table 3
Boo1 Member Star Catalog

Gaia source ID	R.A. (deg)	Decl. (deg)	$u0$	$g0$	$i0$	PMRA (mas yr^{-1})	PMDEC (mas yr^{-1})	$[Fe/H]_{phot}$	Purity	MEM_FLAG[a]	S5_obs[b]	References	CMD_outlier_flag
1231095269513901568	210.02998	15.2386	20.90 ± 0.035	20.17	19.50	0.302	−0.442	−2.44 ± 0.41	0.88	0	1	(a)	0
1230887118218565504	210.0679	14.9441	20.52 ± 0.035	19.75	18.98	0.149	−0.334	−3.01 ± 0.71	0.97	0	1	(a)	0
1231090596588925056	209.7151	15.1449	21.41 ± 0.035	20.67	19.99	0.517	−0.766	−2.31 ± 0.32	0.00	1	1	(a)	0
1230874954871117824	210.1153	14.7380	21.26 ± 0.035	20.47	19.78	0.171	−0.505	−2.03 ± 0.26	0.78	1	1	(a)	0

Notes.
[a] The `MEM_FLAG` numbers are illustrated in Section 4.1.3.
[b] `S5_obs`: `S5_obs` = 1 means this star was observed in S5, and `S5_obs` = 0 means it was not observed in S5.

References. (a) N. Longeard et al. (2022); (b) S. A. Jenkins et al. (2021).

(This table is available in its entirety in machine-readable form in the online article.)

Table 4
Boo2 Member Stars Catalog

Gaia Source ID	R.A. (deg)	Decl. (deg)	$u0$	$g0$	$i0$	PMRA (mas yr^{-1})	PMDEC (mas yr^{-1})	$[Fe/H]_{phot}$	Purity	MEM_FLAG	S5_obs	References	CMD_outlier_flag
3727837759579718272	209.4061	12.8635	18.84 ± 0.035	18.15	17.48	−1.67	0.526	−3.61 ± 0.75	1.	0	0	(b)	1
3727825076541007232	209.4323	12.7905	20.95 ± 0.035	20.21	19.54	−1.569	0.370	−2.26 ± 0.31	0.99	0	0	(b)	0
3728628853900665856	208.4935	12.9786	20.66 ± 0.035	19.96	19.32	−2.076	0.268	−2.25 ± 0.33	0.65	2	0	...	0
3727823118035927936	209.5725	12.8035	21.40 ± 0.035	20.71	20.10	−1.787	−1.205	−2.50 ± 0.75	0.69	3	1	...	0
1230683227532109056	209.2676	13.7516	21.37 ± 0.035	20.75	20.19	−0.596	0.685	−2.5 ± 0.75	0.00	3	0	...	0

References. (a) Koch et al. (2009); (b) J. Bruce et al. (2023); (c) A. P. Ji et al. (2016).

(This table is available in its entirety in machine-readable form in the online article.)

Table 5
Seg1 Member Stars Catalog

Gaia Source ID	R.A. (deg)	Decl. (deg)	$u0$	$g0$	$i0$	PMRA (mas yr^{-1})	PMDEC (mas yr^{-1})	$[Fe/H]_{phot}$	Purity	MEM_FLAG	S5_obs	References	CMD_outlier_flag
621943184658438784	151.7180	16.0433	19.35 ± 0.035	18.74	18.10	−2.017	−1.662	−4. ± 0.75	0.99	0	1	(a, b)	0
621924492960734464	151.7603	15.8487	19.13 ± 0.035	18.36	17.66	−1.898	−1.698	−2.28 ± 0.29	0.99	0	1	(a, b)	0
621925901710013952	151.8407	15.9068	20.97 ± 0.035	20.50	20.18	−2.333	−1.339	−2.68 ± 0.75	0.	1	0	(a)	0
622634296435669376	150.7791	16.0090	20.65 ± 0.035	20.04	19.47	−1.609	1.352	−2.50 ± 0.75	0.86	2	0	...	0
621819764477687296	151.4164	15.5965	20.59 ± 0.035	20.01	19.54	−2.483	−0.394	−2.07 ± 0.54	0.91	2	0	...	0
622820771030434816	151.2795	16.9198	21.33 ± 0.035	20.81	20.42	−1.155	0.165	−2.11 ± 0.79	0.	3	0	...	0
622790908122977920	151.1391	16.7076	21.32 ± 0.035	20.81	20.43	−4.231	−0.581	−2.17 ± 0.88	0.	3	0	...	0

References. (a) J. D. Simon et al. (2011); (b) A. Frebel et al. (2014); (c) J. E. Norris et al. (2010).

(This table is available in its entirety in machine-readable form in the online article.)

ORCID iDs

Anirudh Chiti https://orcid.org/0000-0002-7155-679X
Alex Drlica-Wagner https://orcid.org/0000-0001-8251-933X
Alexander P. Ji https://orcid.org/0000-0002-4863-8842
Guilherme Limberg https://orcid.org/0000-0002-9269-8287
Douglas L. Tucker https://orcid.org/0000-0001-7211-5729

References

Abbott, T. M. C., Abdalla, F. B., Allam, S., et al. 2018, ApJS, 239, 18
Abbott, T. M. C., Adamów, M., Aguena, M., et al. 2021, ApJS, 255, 20
Abdallah, H., Adam, R., Aharonian, F., et al. 2020, PhRvD, 102, 062001
Ahumada, R., Prieto, C. A., Almeida, A., et al. 2020, ApJS, 249, 3
Alvarez, R., & Plez, B. 1998, A&A, 330, 1109
Amorisco, N. C., Zavala, J., & de Boer, T. J. L. 2014, ApJL, 782, L39
Anthony-Twarog, B. J., Laird, J. B., Payne, D., & Twarog, B. A. 1991, AJ, 101, 1902
Astropy Collaboration, Price-Whelan, A. M., Lim, P. L., et al. 2022, ApJ, 935, 167
Astropy Collaboration, Price-Whelan, A. M., Sipőcz, B. M., et al. 2018, AJ, 156, 123
Astropy Collaboration, Robitaille, T. P., Tollerud, E. J., et al. 2013, A&A, 558, A33
Beers, T. C., Preston, G. W., & Shectman, S. A. 1985, AJ, 90, 2089
Belokurov, V., Zucker, D. B., Evans, N. W., et al. 2006a, ApJL, 647, L111
Belokurov, V., Zucker, D. B., Evans, N. W., et al. 2006b, ApJL, 642, L137
Belokurov, V., Zucker, D. B., Evans, N. W., et al. 2007, ApJ, 654, 897
Bernstein, G. M., Abbott, T. M. C., Desai, S., et al. 2017, PASP, 129, 114502
Bertin, E. 2006, in ASP Conf. Ser. 351, Astronomical Data Analysis Software and Systems XV, ed. C. Gabriel et al. (San Francisco, CA: ASP), 112
Bertin, E. 2011, in ASP Conf. Ser. 442, Astronomical Data Analysis Software and Systems XX, ed. I. N. Evans et al. (San Francisco, CA: ASP), 435
Bertin, E., & Arnouts, S. 1996, A&AS, 117, 393
Brown, T. M., Tumlinson, J., Geha, M., et al. 2014, ApJ, 796, 91
Bruce, J., Li, T. S., Pace, A. B., et al. 2023, ApJ, 950, 167
Calore, F., Serpico, P. D., & Zaldivar, B. 2018, JCAP, 2018, 029
Carretta, E., Bragaglia, A., Gratton, R., D'Orazi, V., & Lucatello, S. 2009, A&A, 508, 695
Chiti, A., Frebel, A., Jerjen, H., Kim, D., & Norris, J. E. 2020, ApJ, 891, 8
Chiti, A., Frebel, A., Ji, A. P., et al. 2023, AJ, 165, 55
Chiti, A., Frebel, A., Simon, J. D., et al. 2021, NatAs, 5, 392
Cole, S., Lacey, C. G., Baugh, C. M., & Frenk, C. S. 2000, MNRAS, 319, 168
Czekaj, M. A., Robin, A. C., Figueras, F., Luri, X., & Haywood, M. 2014, A&A, 564, A102
Dall'Ora, M., Robin, A. C., Clementini, G., Kinemuchi, K., et al. 2006, ApJL, 653, L109
Deason, A., Wetzel, A., & Garrison-Kimmel, S. 2014, ApJ, 794, 115
Dotter, A., Chaboyer, B., Jevremović, D., et al. 2008, ApJS, 178, 89
Drlica-Wagner, A., Bechtol, K., Rykoff, E. S., et al. 2015, ApJ, 813, 109
Drlica-Wagner, A., Ferguson, P. S., Adamów, M., et al. 2022, ApJS, 261, 38
Feroz, F., Hobson, M. P., & Bridges, M. 2009, MNRAS, 398, 1601
Filion, C., & Wyse, R. F. G. 2021, ApJ, 923, 218
Flaugher, B., Diehl, H. T., Honscheid, K., et al. 2015, AJ, 150, 150
Frebel, A., Simon, J. D., & Kirby, E. N. 2014, ApJ, 786, 74
Fu, S. W., Simon, J. D., Shetrone, M., et al. 2018, ApJ, 866, 42
Fu, S. W., Weisz, D. R., Starkenburg, E., et al. 2023, ApJ, 958, 167
Gaia Collaboration, Brown, A. G. A., Vallenari, A., et al. 2018, A&A, 616, A1
Gaia Collaboration, Prusti, T., de Bruijne, J. H. J., et al. 2016, A&A, 595, A1
Gaia Collaboration, Vallenari, A., Brown, A. G. A., et al. 2023, A&A, 674, A1
Garling, C., Willman, B., Sand, D. J., et al. 2018, ApJ, 852, 44
Geha, M., Willman, B., Simon, J. D., et al. 2009, ApJ, 692, 1464
Hartley, W. G., Choi, A., Amon, A., et al. 2022, MNRAS, 509, 3547
Hunter, J. D. 2007, CSE, 9, 90
Jenkins, S. A., Li, T. S., Pace, A. B., et al. 2021, ApJ, 920, 92
Jensen, J., Hayes, C. R., Sestito, F., et al. 2024, MNRAS, 527, 4209
Ji, A. P., Frebel, A., Simon, J. D., & Geha, M. 2016, ApJ, 817, 41
Jones, E., Oliphant, T., & Peterson, P., 2001 SciPy: Open Source Scientific Tools for Python, http://www.scipy.org
Keller, S. C., Schmidt, B. P., Bessell, M. S., et al. 2007, PASA, 24, 1
Kim, S. Y., Peter, A. H. G., & Hargis, J. R. 2018, PhRvL, 121, 211302
Koch, A., Wilkinson, M. I., Kleyna, J. T., et al. 2009, ApJ, 690, 453
Koposov, S. E., Belokurov, V., Torrealba, G., & Evans, N. W. 2015, ApJ, 805, 130
Li, T. S., Ji, A. P., Pace, A. B., et al. 2022, ApJ, 928, 30
Li, T. S., Simon, J. D., Kuehn, K., et al. 2018, ApJ, 866, 22
Limberg, G., Queiroz, A. B. A., Perottoni, H. D., et al. 2023, ApJ, 946, 66
Longeard, N., Jablonka, P., Arentsen, A., et al. 2022, MNRAS, 516, 2348
Longeard, N., Jablonka, P., Battaglia, G., et al. 2023, MNRAS, 525, 3086
Longeard, N., Martin, N., Ibata, R. A., et al. 2021, MNRAS, 503, 2754
Malhan, K., Valluri, M., Freese, K., & Ibata, R. A. 2022, ApJL, 941, L38
Martin, N. F., Ibata, R. A., Chapman, S. C., Irwin, M., & Lewis, G. F. 2007, MNRAS, 380, 281
Martínez-Vázquez, C. E., Cerny, W., Vivas, A. K., et al. 2021, AJ, 162, 253
Mau, S., Nadler, E. O., Wechsler, R. H., et al. 2022, ApJ, 932, 128
McConnachie, A. W. 2012, AJ, 144, 4
McConnachie, A. W., & Venn, K. A. 2020, RNAAS, 4, 229
Morganson, E., Gruendl, R. A., Menanteau, F., et al. 2018, PASP, 130, 074501
Muñoz, R. R., Côté, P., Santana, F. A., et al. 2018, ApJ, 860, 66
Munshi, F., Brooks, A. M., Christensen, C., et al. 2019, ApJ, 874, 40
Mutlu-Pakdil, B., Sand, D. J., Walker, M. G., et al. 2019, ApJ, 885, 53
Nadler, E. O., Drlica-Wagner, A., Bechtol, K., et al. 2021, PhRvL, 126, 091101
Norris, J. E., Gilmore, G., Wyse, R. F. G., Yong, D., & Frebel, A. 2010, ApJL, 722, L104
Norris, J. E., Gilmore, G., Wyse, R. F. G., et al. 2008, ApJL, 689, L113
Orkney, M. D. A., Read, J. I., Rey, M. P., et al. 2021, MNRAS, 504, 3509
Ou, X., Chiti, A., Shipp, N., et al. 2024, ApJ, 966, 33
Pace, A. B., Erkal, D., & Li, T. S. 2022, ApJ, 940, 136
Pace, A. B., & Li, T. S. 2019, ApJ, 875, 77
Pan, Y., & Kravtsov, A. 2023, arXiv:2310.08636
Peñarrubia, J., Navarro, J. F., & McConnachie, A.W. 2008, ApJ, 673, 226
Plez, B. 2012, Turbospectrum: Code for Spectral Synthesis, Astrophysics Source Code Library, ascl:1205.004
Pontzen, A., & Governato, F. 2012, MNRAS, 421, 3464
Read, J. I., Agertz, O., & Collins, M. L. M. 2016, MNRAS, 459, 2573
Rimoldini, L., Holl, B., Gavras, P., et al. 2023, A&A, 674, A14
Robin, A. C., Reylé, C., Derrière, S., & Picaud, S. 2003, A&A, 409, 523
Roderick, T. A., Mackey, A. D., Jerjen, H., & Da Costa, G. S. 2016, MNRAS, 461, 3702
Schlegel, D. J., Finkbeiner, D. P., & Davis, M. 1998, ApJ, 500, 525
Simon, J. D. 2019, ARA&A, 57, 375
Simon, J. D., & Geha, M. 2007, ApJ, 670, 313
Simon, J. D., Geha, M., Minor, Q. E., et al. 2011, ApJ, 733, 46
Simon, J. D., Li, T. S., Drlica-Wagner, A., et al. 2017, ApJ, 838, 11
Slater, C. T., Ivezić, Ž., & Lupton, R. H. 2020, AJ, 159, 65
Starkenburg, E., Martin, N., Youakim, K., et al. 2017, MNRAS, 471, 2587
Strutz, T. 2010, Data Fitting and Uncertainty (A Practical Introduction to Weighted Least Squares and Beyond) (Berlin: Vieweg Teubner)
Tarumi, Y., Yoshida, N., & Frebel, A. 2021, ApJL, 914, L10
Tau, E. A., Vivas, A. K., & Martìnez-Vázquez, C. E. 2024, AJ, 167, 57
Taylor, M. B. 2006, in ASP Conf. Ser. 351, Astronomical Data Analysis Software and Systems XV, ed. C. Gabriel et al. (San Francisco, CA: ASP), 666
Usman, S. A., Ji, A. P., Li, T. S., et al. 2024, MNRAS, 529, 2413
van der Walt, S., Colbert, S. C., & Varoquaux, G. 2011, CSE, 13, 22
Vivas, A. K., Martìnez-Vázquez, C., & Walker, A. R. 2020, ApJS, 247, 35
Waller, F., Venn, K. A., Sestito, F., et al. 2023, MNRAS, 519, 1349
Walker, M. G., Mateo, M., Olszewski, E. W., et al. 2009, ApJ, 704, 1274
Walsh, S. M., Willman, B., Sand, D., et al. 2008, ApJ, 688, 245
Wheeler, C., Hopkins, P. F., Pace, A. B., et al. 2019, MNRAS, 490, 4447
White, S. D. M., & Frenk, C. S. 1991, ApJ, 379, 52
Willman, B., Blanton, M. R., West, A. A., et al. 2005a, AJ, 129, 2692
Willman, B., Dalcanton, J. J., Martinez-Delgado, D., et al. 2005b, ApJL, 626, L85
Willman, B., & Strader, J. 2012, AJ, 144, 76
Wolf, J., Martinez, G. D., Bullock, J. S., et al. 2010, MNRAS, 406, 1220